Acta Materialia 188 (2020) 63–78

Contents lists available at ScienceDirect

Acta Materialia

journal homepage: www.elsevier.com/locate/actamat

Full length article

Suppression of shear localization in nanocrystalline Al–Ni–Ce via segregation engineering

Glenn H. Balbus, Fulin Wang, Daniel S. Gianola*

Materials Department, University Of California, Santa Barbara, CA 93106, USA

ARTICLE INFO

Article History:
Received 16 October 2019
Revised 17 December 2019
Accepted 19 January 2020
Available online 24 January 2020

ABSTRACT

Shear localization in nanocrystalline metals is a severely limiting factor precluding their use as practical engineering materials. While several strategies exist to enhance the thermal and mechanical behavior of these materials, there are still many outstanding questions regarding the effects of chemical segregation on shear localization in FCC nanocrystalline materials. In this paper we investigate the mechanical response of a ternary aluminum alloy with a sub-10 nm nanocrystalline microstructure subject to various thermal treatments. Contrary to previous observations, our results suggest that annealing up to 0.7 T_m reduces the propensity for shear localization and increases strength, as demonstrated by a transition in deformation morphology from pronounced strain localization to more homogeneous deformation during indentation. This behavior coincides with the formation of an amorphous intergranular film during annealing, causing intragranular dislocation plasticity to be favored over other grain boundary dominated deformation mechanisms, in turn resulting in a lower propensity for long range plastic localization.

1. Introduction

Nanocrystalline metals have attracted a great deal of interest due to their desirable mechanical properties, such as high hardness [1], fatigue behavior [2], and wear resistance [3,4]. These properties can be attributed to the abundance of grain boundaries, which dramatically affect the physical properties of nanocrystalline materials [1,5]. These boundaries serve a variety of beneficial purposes, such as acting as obstacles to dislocation motion, providing increased strength [6,7], and as efficient sinks for radiation damage [8]. Despite the apparent benefits of these boundaries, nanocrystalline metals are plagued by poor thermal stability, as well as severe plastic instabilities such as catastrophic shear localization [9–11]. The origin of shear localization in nanocrystalline metals has been the subject of much research [9,12] and is most often attributed to the multitude of grain boundary-mediated deformation mechanisms, such as grain rotation and sliding [5,13], operative in nanocrystalline metals. The plurality of deformation mechanisms has been shown to induce strain-softening behavior and facilitate long range localization in materials with extremely small grain sizes (< 15 nm) via strain partitioning [12].

Careful alloying strategies can help mitigate thermal instabilities in pure nanocrystalline metals [14–27], as well as provide additional strength [28,29]. The most common approach is to introduce alloying elements that exhibit a strong propensity for segregation to grain boundaries [27]. The presence of these highly segregating elements at grain boundaries can kinetically pin the boundaries [30] or decrease the grain boundary energy [27]. Classical formulations give grain boundary velocity [31] as proportional to both the thermodynamic driving force (i.e. grain boundary energy) and a kinetic factor, thus both energetic and kinetic efforts to stabilize the grain boundary can effectively reduce the grain boundary velocity under thermal excitation. This alloying strategy has been used quite successfully for promoting thermal stability, enabling the design of nanocrystalline alloys that are resistant to coarsening up to high temperatures, such as Cu–Ta [30], Ni–W [32], and W–Ti [26].

Solute segregation to grain boundaries has been shown to have a pronounced effect on mechanical properties as well. The presence of both metal and nonmetal dopants at grain boundaries promotes increased strength while mitigating some mechanical instabilities, such as stress-driven coarsening [33,34]. Hu, et al. [7] demonstrated that grain boundaries of electrodeposited Ni–Mo can be stabilized by the addition of higher concentrations of Mo, followed by low-temperature annealing to cause segregation to grain boundaries. In doing so, a transition from so-called inverse Hall–Petch behavior at low Mo content where a reduction in grain size leads to a decrease in the flow stress [11,35] to classical Hall–Petch behavior at high Mo content was observed. While many studies have demonstrated substantial increases in strength due to alloying, the plastic deformation behavior of these materials is often undesirable. Indentation, pillar

* Corresponding author.
E-mail address: gianola@ucsb.edu (D.S. Gianola).

https://doi.org/10.1016/j.actamat.2020.01.041
1359-6454/

compression, and tension testing of stable nanocrystalline metals, such as Ni and Ti based alloys [11,36–38], show strong shear localization immediately after the onset of plasticity.

Not only do alloying additions at grain boundaries affect the properties of nanocrystalline metals, but structural transitions of the grain boundaries due to chemical segregation have pronounced effects on the thermal and mechanical behavior of nanocrystalline metals as well [39]. Nanocrystalline materials with a variety of grain boundary structures, ranging from atomistically sharp with various fractions of special grain boundaries [40] to completely amorphous grain boundaries [41] have been produced. In particular, the effects of amorphous intergranular films on the mechanical response of nanocrystalline metals can be quite pronounced. Khalajhedayati et al. [42] have shown that the presence of an amorphous intergranular film in a nanocrystalline Cu–Zr alloy yields a four-fold increase in ductility, with little to no degradation in strength. Amorphous intergranular films provide mechanical stability by providing sinks for dislocations that propagate across the crystalline regions of the material, as well as strong pinning points as dislocations traverse the grain interior [43–45]. In order to design alloys that can exhibit amorphous intergranular films, several key criteria have been proposed: high degree of chemical complexity, large atomic radius mismatch, negative enthalpy of segregation, and a positive enthalpy of mixing [46]. All of these criteria, apart from the negative enthalpy of segregation, echo those proposed for designing fully amorphous alloys [47].

In addition to the spatial extent of the grain boundary, the local atomistic structure – the position of solutes at the grain boundary [34], the structural motifs of the boundary [39], and disconnection density [48,49] – play a large role in both the strength and propensity for shear localization of nanocrystalline metals. These subtle differences in grain boundary structure and energy are often referred to as grain boundary state. The grain boundary state of nanocrystalline metals may be relaxed through annealing at low temperatures, which provides increases in strength with negligible changes in grain size [7,50]. While the effects of low temperature annealing are easily understood in alloys prone to chemical segregation to grain boundaries, anneal hardening can occur in nominally pure or weakly segregating systems. Rupert and others [36,50] demonstrated that low temperature annealing strongly increases the hardness and yield strength of electrodeposited Ni–W, which has a weak tendency for chemical segregation. Renk et al. [51] observed this behavior in a chemically complex steel, and utilized atom probe tomography to rule out the role of chemical segregation. Others have noted that there may be processing routes to rejuvenate grain boundaries isochemically at the expense of mechanical strength, potentially decreasing the propensity for shear localization [52]. By annealing nanocrystalline Ni–W, Khalajhedayati and Rupert reported substantial increases in strength along with decreases in strain-to-failure after thermal relaxation [36]. This decrease in strain to failure is concomitant with an increased propensity for catastrophic shear localization in pillar compression experiments. These authors suggest the degree of relaxation of the boundaries – intricately linked to the thermal history of the material – governs the propensity for shear localization: the more relaxed, the higher susceptibility for localization. This behavior has also been shown in molecular dynamics simulations, where annealing of grain boundary regions leads to increased strength and more localized deformation [53].

Taken as a whole, it is clear that the details of the grain boundary ranging from atomic structure, chemical ordering, and structural/energetic state are crucial for understanding the mechanical performance of nanocrystalline metals, particularly the propensity for localization. While several detailed studies exist both experimentally [11,36,50] and computationally [53], there are several outstanding questions regarding the role of solute segregation on shear localization in nanocrystalline metals. For instance, can the tradeoff between strength and tendency for shear localization observed in previous studies [11,36] be overcome via segregation engineering? In this paper we investigate the mechanical response of a ternary aluminum alloy with a sub-10 nm grain size subject to various thermal treatments. Our results suggest that traditional relaxation annealing dramatically reduces the propensity for shear localization, along with significant increases in strength. This counter intuitive result is evident in a dramatic transition in deformation morphology from strong strain localization to more homogeneous deformation during indentation.

2. Alloy design

We initially focus our attention on designing a ternary Al-based nanocrystalline alloy that exhibits co-segregation of alloying additions to grain boundaries. These properties will enable us to investigate the effects of segregation on shear localization in a multicomponent system.

Multicomponent nanostructured Al alloys have been reported in studies of partially crystallized amorphous alloys, which exhibit desireable properties such as high strength and low density [54–58]. In amorphous Al-based alloys, combinations of transition (TM) and rare earth (RE) metals are frequently used as alloying additions to increase the complexity of crystallization products, thereby increasing the glass formability of these systems [57]. Al-TM-RE alloys have high strength [59] and a variety of unique microstructures [57]. While the Al-TM-RE alloy space is quite broad, we turn our focus to the Al-Ni-RE ternary system. Multiphase Al-Ni-RE crystalline alloys exhibit desirable solidification microstructure formed during casting, as well as their thermomechanical properties owing to thermally stable nanoscale precipitates [58]. Various RE elements have been studied in these systems, but Ce is promising for a variety of reasons. Binary Al–Ce alloys are being investigated as promising alloys for additive manufacturing due to the high thermal stability, as well as relative abundance of Ce from various RE production [60]. The thermal and mechanical behavior of amorphous Al–Ni–Ce alloys have been characterized quite extensively [55–57,59,61–63], and exhibit thermal behavior that is desirable for a nanocrystalline system. After annealing at low temperatures, Al–Ni–Ce amorphous alloys first crystallize through the nucleation of FCC-Al particles in an amorphous matrix [62]. Then, due to the negligible solubility of Ce and Ni in FCC-Al, these elements are rejected into the amorphous material surrounding the FCC-Al nuclei. This strong elemental segregation of Ni and Ce away from crystalline Al suggests that these may be suitable alloying additions for a nanocrystalline Al alloy. We hypothesize that a single phase nanocrystalline Al–Ni–Ce based alloy may exhibit both enhanced thermal and mechanical stability due to the strong tendency for Ni and Ce to segregate during low temperature annealing, as well as the potential for the formation of amorphous intergranular films due to the overall glass formability of this alloy space [27,46].

3. Materials and methods

Nanocrystalline Al–Ni–Ce samples were prepared by confocal DC magnetron sputtering in an AJA ATC 1800 Sputter deposition system equipped with 2-inch diameter sputter sources. Depositions were performed using two targets: one Al (99.999% purity) target and one pre-alloyed $Al_{87}Ni_7Ce_6$ target (composition noted in at%, 99.95% purity). Power densities of 4.93 W cm^{-2} and 8.63 W cm^{-2} were used for the Al and $Al_{87}Ni_7Ce_6$, respectively. Base pressures below 10^{-7} Torr were attained prior to each deposition, and all depositions were performed at a processing pressure of 3 mTorr in Ar at room temperature. The deposition rate was measured to be 0.27 nm s^{-1} using an Inficon quartz crystal monitor. An interrupted deposition procedure was utilized to achieve the desired nanocrystalline microstructure, wherein the targets were shuttered every 36 s for 5 s. This

technique enables the deposition of films with very fine grain sizes by suppressing grain growth during continuous deposition, as has been reported elsewhere [64–66]. This deposition procedure resulted in an approximate thickness of 10 nm per deposition interval. For comparison, pure Al samples were prepared in the same manner, using only the Al target at a power density of 12.3 W cm^{-2}. Thick (1 μm) samples were deposited on Si (100) wafers for mechanical characterization, and thin (40 nm) samples were deposited onto Cu transmission electron microscopy (TEM) grids with C support films for (S)TEM analysis. Thin samples were characterized via (S)TEM in a Thermo Fisher Talos G2 200X STEM operating at 200 kV. The nominal composition of the Al-Ni-Ce sample was measured by SEM-EDS, which is typically accurate to within 5 at%.

Annealing experiments on both thin and thick samples were performed under vacuum ($< 10^{-7}$ Torr) in the deposition chamber. A slow ramp rate of 0.1 °C s^{-1} was used to reach the desired temperature, wherein the samples were held for 1 hr. The heater was then shut off and the system was allowed to cool slowly under vacuum over the course of 2–3 h. Both thick and thin samples were heated to temperatures of 200 °C, 325 °C, and 380 °C.

Nanoindentation experiments on the thick samples were performed using a Nanomechanics iMicro Nanoindenter equipped with a 50 mN load cell. Hardness measurements were performed with a Berkovich tip diamond indenter at a variety of indentation strain rates. The tip area function of the Berkovich tip was calibrated on fused silica before all experiments. All data was collected using the continuous stiffness method (CSM) [67], where a dynamic oscillation is superimposed during loading to measure hardness and elastic modulus as a function of depth. All experiments were performed using a 2 nm dynamic displacement at a frequency of 100 Hz. Each data point reported below corresponds to at least 20 indentations. Constant strain rate indentation tests were also performed at a series of indentation strain rates to elucidate the strain-rate sensitivity exponent and activation volume of samples subjected to various isochronal-isothermal anneals.

The surface morphology of the thick samples near the indentation experiments was imaged in an FEI Teneo FESEM. As deposited samples of the Al and $Al_{85}Ni_{10}Ce_5$ were imaged at an accelerating voltage of 5 kV using the Everhart-Thornley detector. Annealed $Al_{85}Ni_{10}Ce_5$ were imaged at an accelerating voltage of 2 kV using an in-column detector (T1), which is very sensitive to surface topography. Cross-sectional electron transparent samples were extracted from indents in the as-deposited and 200 °C annealed state. These samples were prepared using a FEI Helios Dualbeam Nanolab 650 focused ion beam (FIB) with a final ion polishing step at 5 kV, 16 pA to remove FIB-induced damage. Sample thicknesses were approximately 100 nm. TEM investigations of samples prepared using the FIB were performed using a FEI Tecnai G2 Sphera operated at 200 kV.

4. Results

4.1. Microstructural comparison to pure Al

High angle annular dark field (HAADF) STEM micrographs from the thin as-deposited $Al_{85}Ni_{10}Ce_5$ samples shown in Fig. 1a demonstrate the extremely fine microstructure produced during the interrupted sputtering of our highly alloyed Al-based system. Conversely, the bright field STEM micrograph of the pure Al (Fig. 1b) exhibits a much larger grain size. Using dark field (DF) TEM for the $Al_{85}Ni_{10}Ce_5$ and annular dark field STEM for the pure Al, grain size distributions were measured (Fig. 1c). Average grain sizes of 28 ± 11 nm for the pure Al sample and 7.6 ± 2 nm for the $Al_{85}Ni_{10}Ce_5$ were measured. As the thin specimens are only ≈ 40 nm thick, the grain size of the pure Al sample is slightly larger than half of the film thickness, a

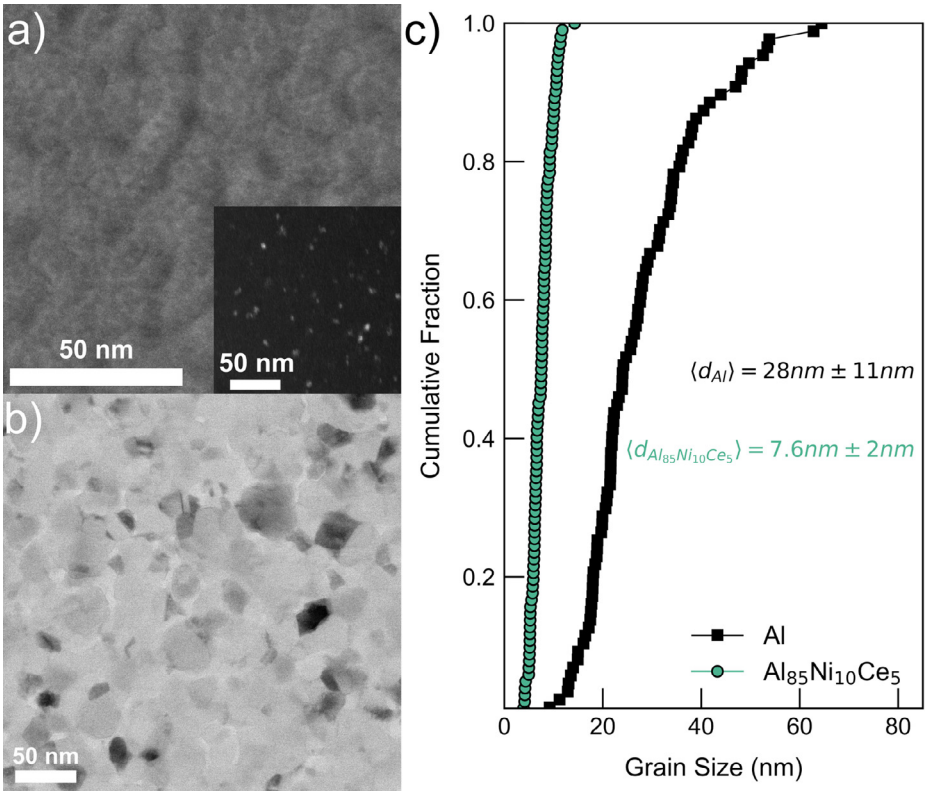

Fig. 1. STEM micrographs and corresponding grain size distributions of thin samples on C-TEM grids. (a) HAADF STEM image of the as-deposited $Al_{85}Ni_{10}Ce_5$, (b) BF STEM image of the Al sample, and (c) grain size statistics generated from DF TEM images of the $Al_{85}Ni_{10}Ce_5$, and annular DF STEM images of the Al. The inset in (a) is a corresponding DF image of the as-deposited $Al_{85}Ni_{10}Ce_5$.

common observation for sputtered films at relatively high homologous temperatures [68]. The HAADF micrograph of the as-deposited $Al_{85}Ni_{10}Ce_5$ exhibits relatively uniform contrast with small domains outlined in regions of higher contrast, presumably Al enriched in Ni and Ce given the atomic number contrast [69]. The size of domains observed in the HAADF image correspond to the grain size measured from DF TEM imaging. Due to the negligible solubility of either Ni or Ce in Al [55,56], and the high homologous temperature of Al at room temperature, moderate segregation of these elements to grain boundaries in the as-deposited microstructure is expected.

Selected area diffraction (SAD) patterns taken with a 10 μm diameter aperture (Fig. 2a and b) demonstrate a single-phase FCC structure for both the pure Al and $Al_{85}Ni_{10}Ce_5$. The SAD pattern from the pure Al exhibits several distinct spots resulting from diffraction of individual grains, rather than a continous ring, due to the larger grain size (see Fig. 1c). Given the high glass formability of this alloy, the absence of a typical amorphous halo in the diffraction pattern of the $Al_{85}Ni_{10}Ce_5$ is surprising. To further analyze any structural differences between pure Al and $Al_{85}Ni_{10}Ce_5$, the radially integrated intensity of the diffraction patterns is shown in Fig. 2c. We observe only a small broadening of the {111} peak in the $Al_{85}Ni_{10}Ce_5$ sample and presence of higher order planes in the diffraction pattern, suggesting that the sample is predominantly crystalline. Further examination of Fig. 2c indicates a small shift in the peak locations in the $Al_{85}Ni_{10}Ce_5$ compared to the pure Al. Using Gaussian peak fitting of the {111} peak location, we measure a lattice parameter of 4.065 for the $Al_{85}Ni_{10}Ce_5$ sample, corresponding to a ≈0.5% lattice expansion compared to pure Al (dashed lines in Fig. 2d). This suggests the formation of a non-equilibrium, supersaturated solution of Ni and Ce in a nanocrystalline Al microstructure – a feature often reported in alloys prepared via sputter deposition [68,70].

While these results are indicative of the behavior of the 40 nm thick films, we do not observe significant differences between these and the 1 μm thick $Al_{85}Ni_{10}Ce_5$ films. As will be discussed in Section 4.4, the average grain size and composition measured from the cross-sectional TEM observations of the thick $Al_{85}Ni_{10}Ce_5$ films are nearly identical to those measured in Fig. 1. Similar studies on nanocrystalline Al alloys [33,71] have also demonstrated that, while there may be a slight difference in the grain aspect ratio of thicker films compared to plan view TEM samples, the microstructures are otherwise comparable. Thus, we posit that observations made on thin $Al_{85}Ni_{10}Ce_5$ specimens can be extended to that of the thick films.

4.2. Mechanical properties in comparison to pure Al

The mechanical properties of thick samples (both pure Al and $Al_{85}Ni_{10}Ce_5$) deposited onto Si (100) wafers were measured by nanoindentation. Fig. 3 shows representative indentation morphologies observed in the SEM, along with load-displacement data from 20 indentations performed on each of these samples. These experiments were performed at an indentation strain rate of 0.1 s^{-1} to a fixed depth of 500 nm. The indented $Al_{85}Ni_{10}Ce_5$ shown in Fig. 3a exhibits profuse shear band formation both in the pileup region as well as beneath the indenter. This behavior during indentation experiments, often observed of amorphous metals, is rarely observed in crystalline materials. The presence of these shear bands in the indented $Al_{85}Ni_{10}Ce_5$ will be discussed in great detail in Section 5.1. The hardness values of the pure Al and the $Al_{85}Ni_{10}Ce_5$ are 0.99 ± 0.19 GPa and 4.67 ± 0.24 GPa, respectively. These values were extracted from a depth of 100 nm to minimize any influence from the substrate. While residual stresses can affect the mechanical properties measured during indentation [72], these differences arise due to contact area discrepancies, and disappear when the contact area is corrected. Using the final contact area measured in the SEM (Fig. 3a), we estimate an error of less than 0.5% between the hardness reported in Fig. 3c using the CSM technique and the hardness calculated using the final load and contact area measured in SEM. It is clear from Fig. 3b that the pure Al film is quite rough, and the average grain size in the pure Al thick films is likely larger than reported in Fig. 1. The surface roughness is consistent with other observations of sputtered Al films, particularly those sputtered at high rates [33,68,71]. The large grain size is likely due to the absence of any alloying elements or impurities which would serve to pin the grain boundaries and preserve the small grain size during deposition of the pure Al. For pure metals, the grain size is typically dependent upon the thickness of the film, which explains the apparent discrepancy [68]. This behavior is not observed in systems with alloying additions to stabilize the grain size, such as the $Al_{85}Ni_{10}Ce_5$ (see additional observations in Section 4.4).

4.3. Annealing effects on Al–Ni–Ce

To study the effects of annealing on the nanocrystalline $Al_{85}Ni_{10}Ce_5$, particularly the tendency for co-segregation of Ni and Ce to grain boundaries and the subsequent mechanical behavior, both the thick and thin samples were subjected to isochronal-isothermal annealing at 200 °C, 325 °C, and 380 °C. Micrographs of the as-deposited sample and those annealed at 200 °C and 325 °C (Fig. 4a–c) were

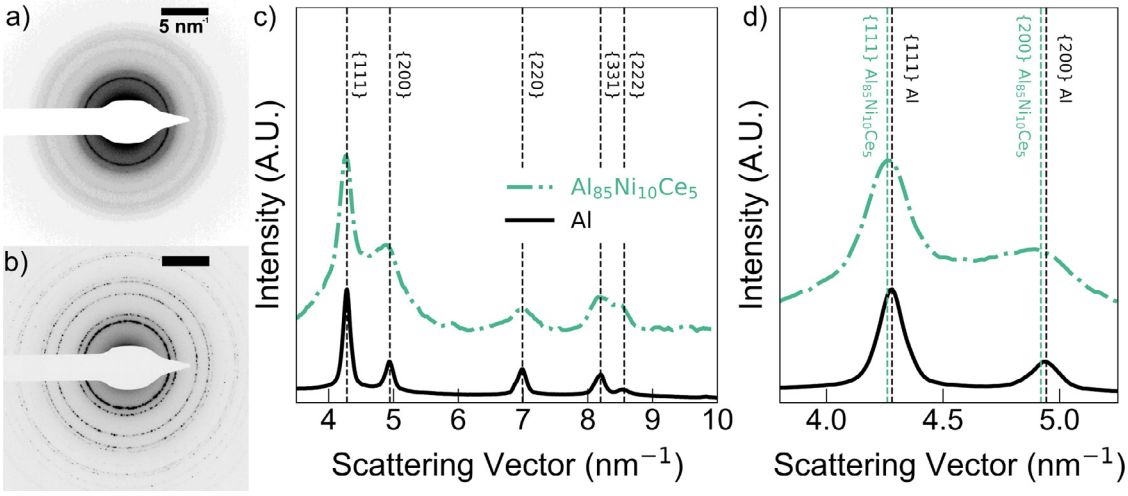

Fig. 2. (a,b) Diffraction patterns taken from the thin $Al_{85}Ni_{10}Ce_5$ and Al samples. (c,d) corresponding integrated azimuthal intensity.

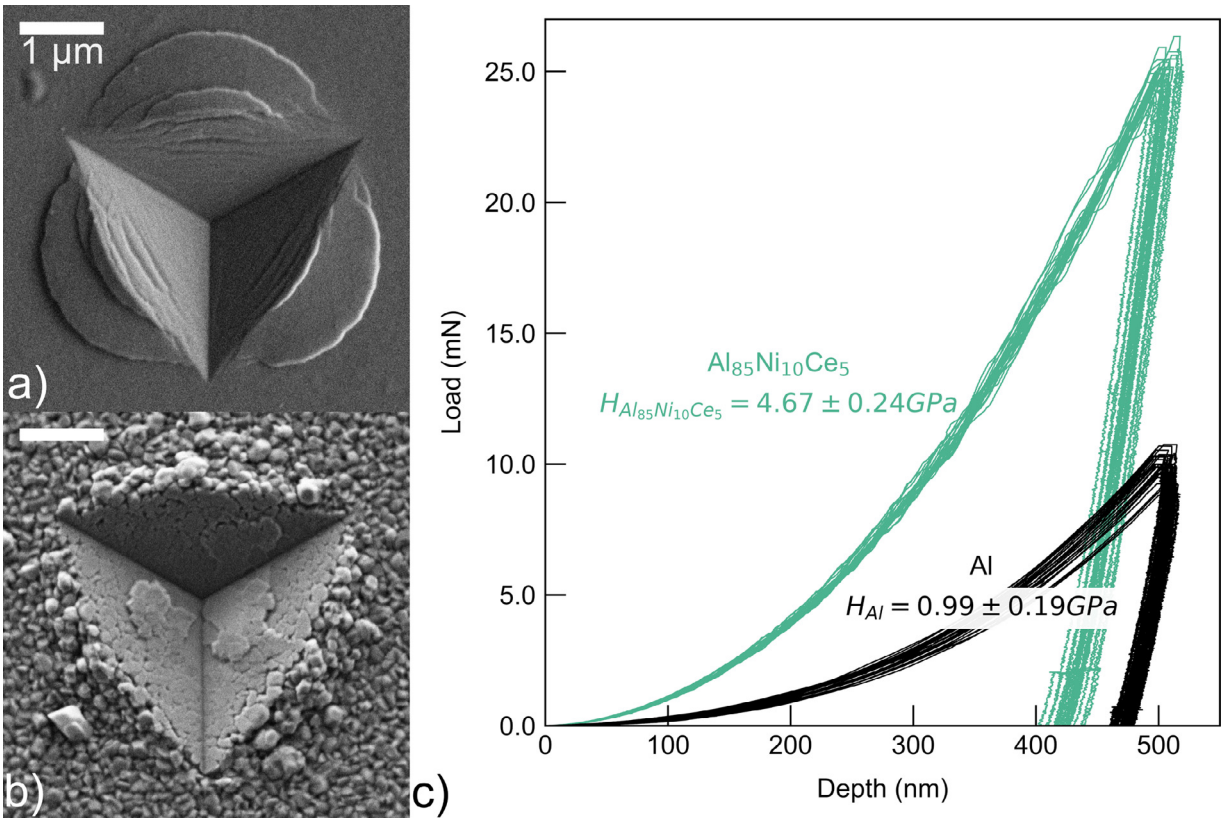

Fig. 3. Indentation morphology observed in SEM of thick (a) as-deposited $Al_{85}Ni_{10}Ce_5$ and (b) Al samples, along with corresponding load-depth curves (c).

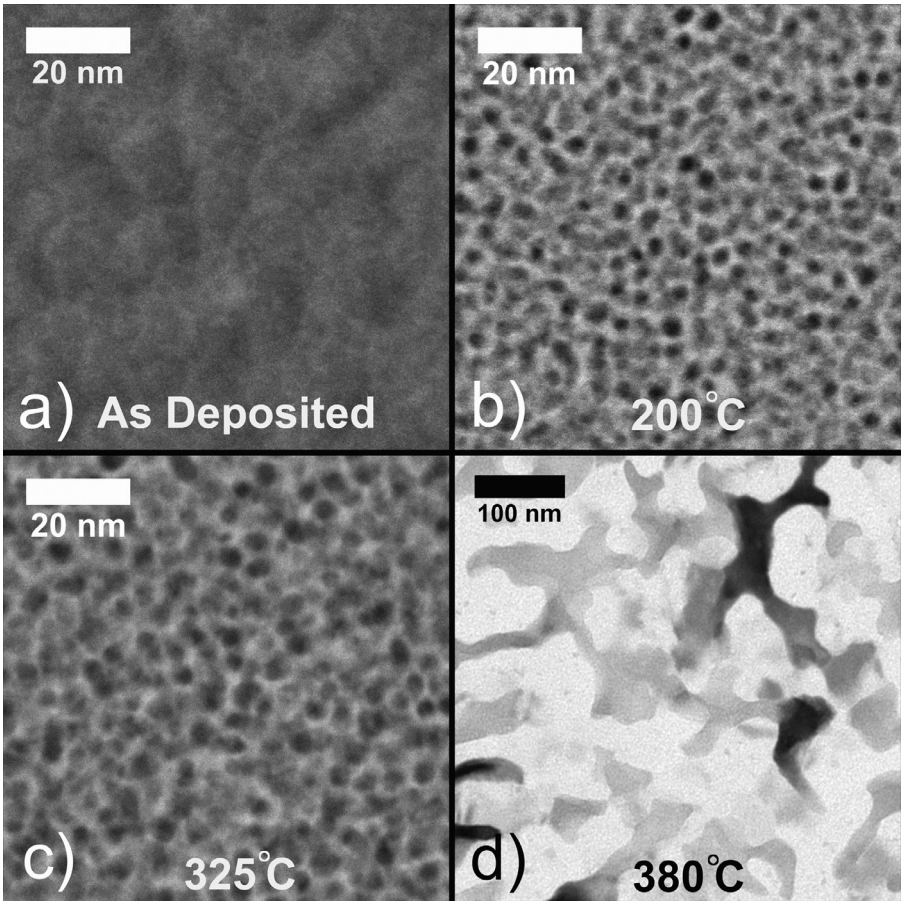

Fig. 4. Microstructure of the thin samples on C-TEM grids in the (a) as-deposited state, and subjected to annealing at (b) 200 °C, (c) 325 °C and (d) 380 °C. (a–c) are HAADF STEM images, whereas (d) is a BF TEM image.

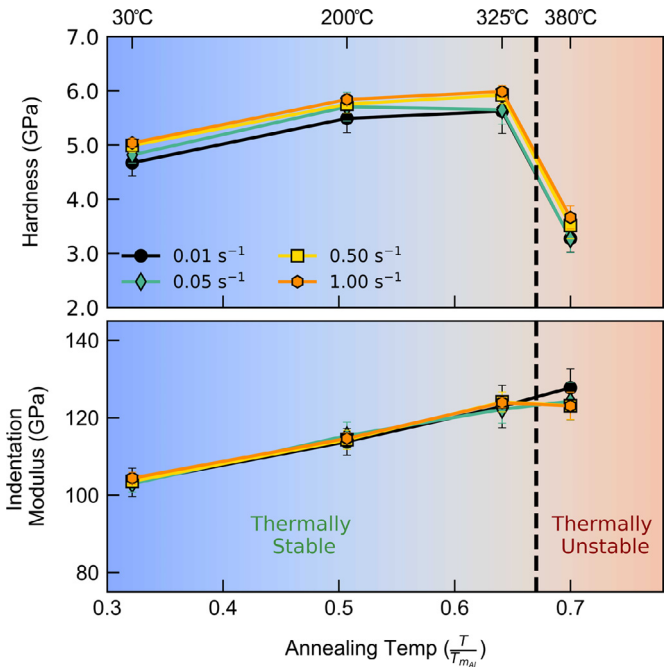

Fig. 5. Indentation hardness and modulus measured after various isochronal-isothermal annealing, at various nominal indentation strain rates.

acquired using HAADF STEM imaging, whereas the sample annealed to 380 °C (Fig. 4d) was imaged using conventional bright field TEM. It is clear from the microstructural images in (Fig. 4a–c) that annealing up to 325 °C induces strong chemical segregation with negligible grain coarsening. This segregation behavior is consistent with the literature on amorphous Al–Ni–Ce alloys, where diffusion of Ni and Ce away from FCC-Al nuclei precedes second phase precipitation [55,56]. At temperatures above 380 °C, intermetallic phases such as Al_3Ni and $Al_{11}Ce_3$ [63] begin to precipitate out and the microstructure coarsens rapidly to form the eutectic microstructure observed in Fig. 4d.

Mechanical properties of the thick samples subjected to identical annealing procedures were probed using nanoindentation. These indentation experiments were performed at strain rates varying from 0.01 s^{-1} to 1.00 s^{-1}. Indentation hardness and modulus values, extracted from 100 nm depths for all samples and strain rates tested, are presented in Fig. 5. We observe that at temperatures below 380 °C, there is an increase in both hardness ($\Delta H = 0.95$ GPa) and modulus ($\Delta E = 20$ GPa). At 380 °C, the hardness begins to decrease, concomitant with the microstructural coarsening observed in Fig. 4d. Fig. 6 shows the hardness as a function of nominal indentation strain rate, along with corresponding activation volume $\left(v = 3\sqrt{3}\frac{\partial \log \dot{\epsilon}}{\partial H}\right)$ and strain rate sensitivity exponent $\left(m = \frac{\partial \log H}{\partial \log \dot{\epsilon}}\right)$ for each annealing temperature. The m values and activation volumes were calculated as described by Maier et al. [73]. Values for ultra-fine grained Al, nanocrystalline Ni, and nanocrystalline 316L steel are included as a reference [74,75]. While inertial effects are quite important at high indentation strain rates, we noticed an insignificant ($<$ 5%) change when comparing either the activation volume or m values calculated from only the slowest strain rates ($<$ 0.1 s^{-1}) to those calculated over the entire range measured.

The microstructural evolution observed in Fig. 4 is consistent with the change in hardness observed in Fig. 5 (as noted above), as well as the strain rate sensitivity behavior in Fig. 6. Prior to the onset of microstructural coarsening (i.e. at annealing temperature below 380 °C), we observe an increase in hardness of ≈1 GPa along with strong chemical segregation, a phenomena termed segregation hardening [7,27,76]. The activation volumes in Fig. 6b of ≈8 b^3, prior to the onset of coarsening, suggest that grain boundary mediated deformation mechanisms are operative. While we do observe an increase in the strain rate sensitivity exponent after the onset of coarsening, the values of both m and v after coarsening are still in the grain boundary mediated deformation regime ($v = 5–50b^3$,

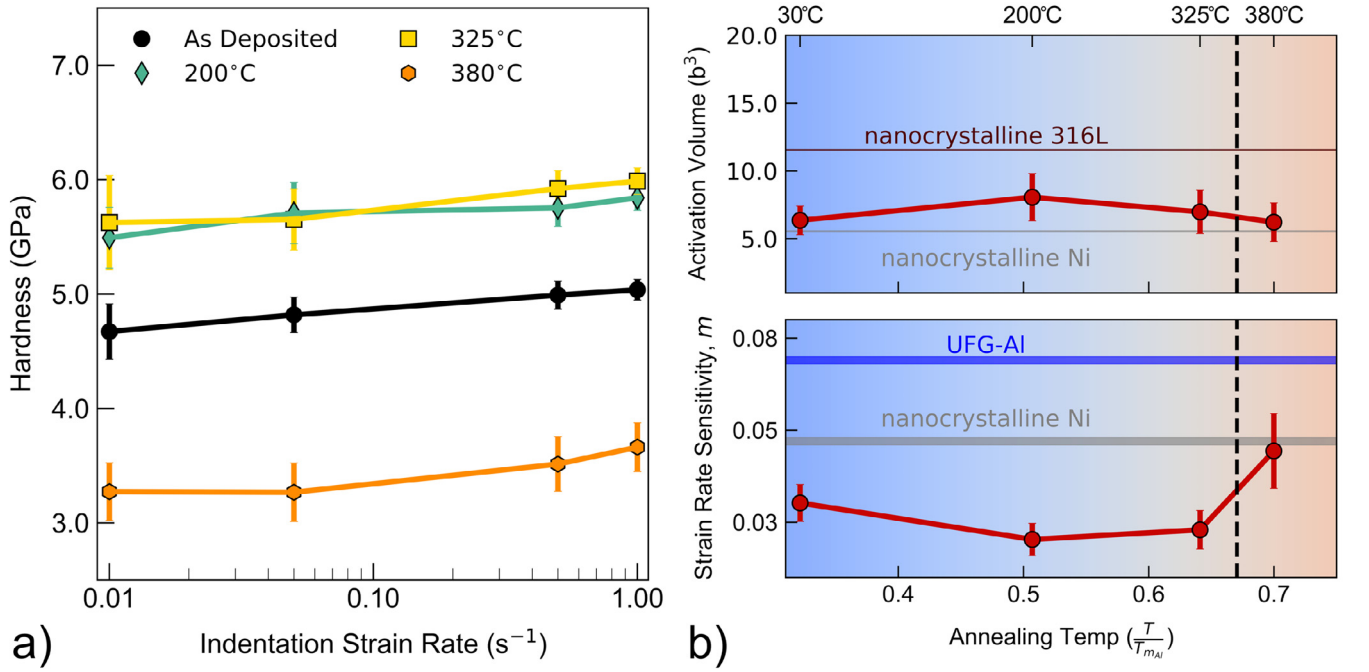

Fig. 6. (a) Indentation hardness as a function of nominal indentation strain rate plotted for each different annealing temperature. (b) Strain rate sensitivity exponent m and corresponding activation volume extracted from the data presented in (a). Error bars in (b) correspond to 95% confidence intervals. Data for UFG Al, nanocrystalline Ni, and nanocrystalline 316L are from Refs [74,75].

$m = 0.01-0.1$). This is consistent with the microstructural evolution presented in Fig. 4, as the microstructure retains a nanoscale eutectic structure after precipitation. These values are also consistent with reports of rapidly solidified or cast alloys with similar compositions [58,59].

The microstructures in Fig. 4 suggest that a spatially extended grain boundary region develops as a result of chemical segregation. Using HAADF images acquired using identical camera settings (Fig. 4) and applying identical image thresholding, the minimum distances between neighboring grains was measured for at least 50 grains in each annealing condition. Corresponding distributions of the widths of the spatially extended grain boundary regions for samples annealed at 200 °C and 325 °C are presented in Fig. 7. The widths of the as-deposited sample were difficult to resolve given the uniform contrast of the image, and were all quite thin (< 0.5 nm), so a vertical dashed line at 0.5 nm is included as an upper bound for the widths of the grain boundaries in the as-deposited condition. While the detailed TEM procedures established by Dillon et al. [77] are necessary for identifying specific types of grain boundary structures, establishing an appropriate diffraction condition for samples with many grains through the thickness was not possible for these samples. Nevertheless, the analysis presented in Fig. 7 indicates that both the 200 °C and 325 °C annealed samples have a mean grain boundary width of 1.0 nm and standard deviation of 0.4 nm, suggesting a transition from an ordered grain boundary in the as-deposited condition to an amorphous intergranular film after annealing. A nano-beam electron diffraction pattern of the 325 °C annealed sample taken with a 10 nm diameter probe size is included as an inset in Fig. 7 to better elucidate the local structure [78]. The probe size utilized when collecting this diffraction pattern is larger than the maximum grain size, thus the diffraction pattern contains information both from the inter- and intragranular regions. The diffraction pattern shown in Fig. 7 exhibits both prominent crystalline peaks and an amorphous halo suggestive of the formation of an amorphous intergranular film after annealing. This amorphous halo is unlikely to arise due to surface oxides or carbonaceous layers, all of which manifest at smaller reciprocal space vectors and would thus be obscured by the beam-stop [79]. Surprisingly, these amorphous intergranular films are expected to be in equilibrium at high temperature and require fast quenching to be preserved at room temperature [41]. It appears that in this system, either due to spatial confinement or the good glass formability of the Ni and Ce enriched zone, the critical cooling rates are lower in this alloy.

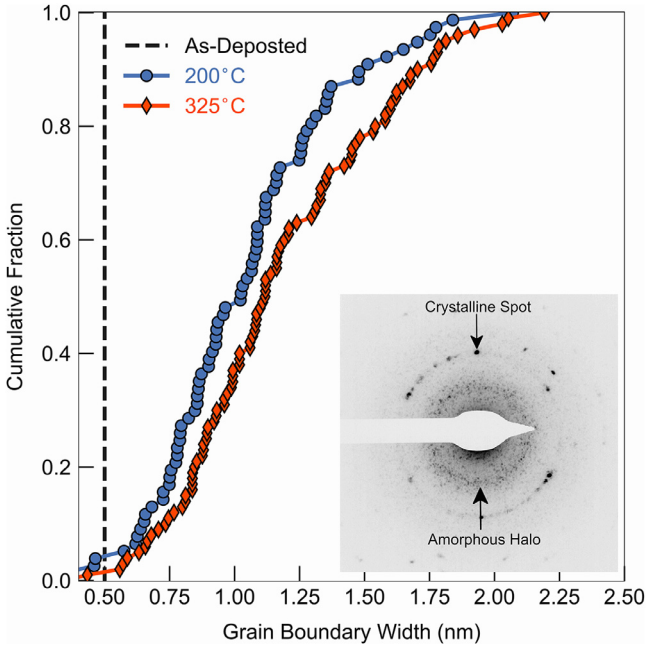

Fig. 7. Distribution of grain boundary widths measured from micrographs of the 200 °C and 325 °C annealed samples in Fig. 5. The vertical dashed line indicates the maximum grain boundary width measured for the as-deposited condition. The inset is a nano-beam diffraction pattern generated from the 325 °C sample, showing indications of a crystalline and amorphous structure.

4.4. Indentation deformation microstructure

To better understand the hardening observed prior to coarsening, particularly its effect on the deformation morphology, SEM micrographs of representative indentations from samples annealed up to 325 °C are presented in Fig. 8. The as-deposited $Al_{85}Ni_{10}Ce_5$ exhibits profuse shear localization both under the indenter and in the pileup region (Fig. 3a, Fig. 8a). Fig. 8b shows the indentation morphology after annealing at 200 °C for 1 h, where the shear localization in the pileup region has diminished quite substantially, but distinct semi-circular shear offsets are still present. After annealing at 325 °C for 1 h (Fig. 8c), shear localization in the pileup region is minimal and almost completely eliminated, which occurs alongside increasing hardness (Fig. 5).

To fully characterize the transition in deformation morphology observed in Fig. 8 due to annealing, including any induced grain growth or rotation, TEM lamella were extracted from the as-deposited and 200 °C annealed sample, as shown in the inset in Fig. 9a. Fig. 9a shows a bright field (BF) TEM image of the representative microstructure of the as-deposited film far away from the indent. The development of a slight elongation of the grains in the growth direction of the film (up in Fig. 9a) is observed. Fig. 9b shows a BF TEM image from under the indent of the as-deposited $Al_{85}Ni_{10}Ce_5$, showing several regions of dark contrast emanating out from beneath the indenter. These are regions where many grains have rotated into a diffraction condition that would not be illuminated in BF imaging. No obvious grain coarsening under the indent was observed in any of these regions, in contrast to other reports [80].

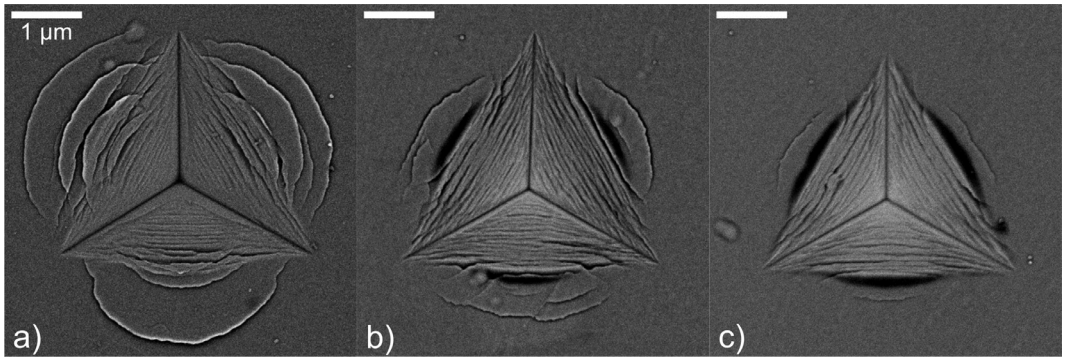

Fig. 8. Indentation morphologies of $Al_{85}Ni_{10}Ce_5$ samples in the (a) as-deposited, (b) 200 °C and (c) 325 °C annealed state.

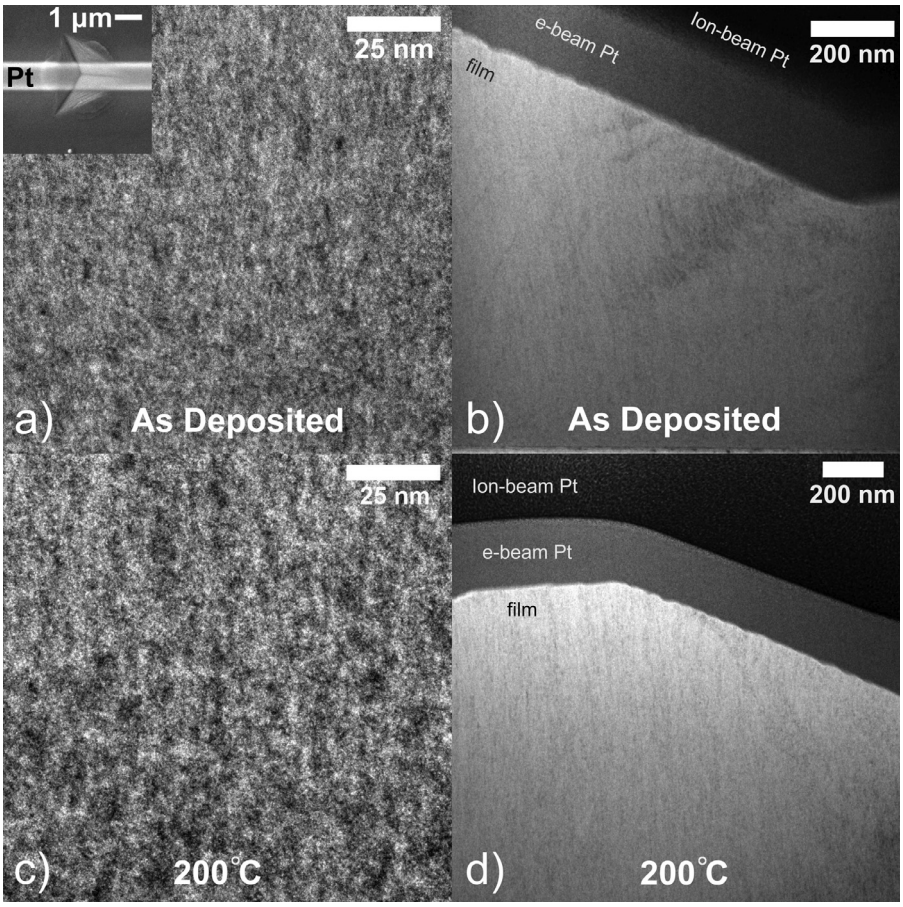

Fig. 9. BF TEM micrographs of TEM lamella extracted from near an indent in the (a),(b) as-deposited $Al_{85}Ni_{10}Ce_5$ and (c),(d) the 200 °C annealed $Al_{85}Ni_{10}Ce_5$. (a) and (c) were acquired far away from the indentation, whereas (b) and (d) are directly beneath the indent. The inset in (a) shows the geometry for extraction of the lamella, where the bright horizontal region is the Pt layer deposited to minimize Ga+ damage during sample preparation in the FIB.

BF TEM images of the lamella extracted from underneath an indent in the 200 °C annealed sample are shown in Fig. 9d. The undeformed microstructure of the 200 °C annealed sample (Fig. 9c) exhibits the same grain size and morphology (i.e. slight elongation in the growth direction) as the undeformed, as-deposited film (Fig. 9a). The deformed microstructure of the 200 °C annealed sample (Fig. 9d) exhibits two faint dark regions underneath the indenter where grains have rotated. However, the dark regions in the 200 °C annealed sample (Fig. 9d) are oriented differently from those in the as-deposited material (Fig. 9b). The regions in the 200 °C annealed sample (Fig. 9d) are nearly perpendicular to those observed in the as-deposited sample (Fig. 9b), which align normal to the surface of the indent. This localized reorientation will be discussed in detail in Section 5.3.

Diffraction patterns of these samples were taken from two regions far away from the indent to characterize the texture in the undeformed sputtered films, and beneath the indent (Fig. 10). The selected area is schematically represented in the insets in Fig. 10a and b. The undeformed as-deposited and 200 °C annealed samples exhibit six distinct spots originating from diffraction of {111} planes (Fig. 10a and c). This texture corresponds to a predominant {111} texture in the growth direction of the film, which is consistent with sputtering fiber texture reported in the literature for other FCC metals [68]. We observe little difference between the two undeformed microstructures, which is consistent with the thermal behavior of the thin samples (Fig. 4 a and b). However, there is a clear difference between the diffraction patterns of the as-deposited and 200 °C deformed material (Fig. 10b and d). Both the as-deposited (Fig. 10b) and 200 °C annealed (Fig. 10d) diffraction patterns show clear grain rotation as a result of the deformation induced by the indenter, yet the specifics of the rotation clearly differ between the two samples. The 200 °C annealed diffraction pattern (Fig. 10d) appears to have undergone a rigid rotation – i.e. a majority of grains in the 200 °C annealed samples giving rise to the diffraction pattern in Fig. 10c have rotated by a fixed amount. Conversely, the as-deposited material (Fig. 10b) exhibits significant streaking of the diffraction spots, indicating that many grains remain in their initial orientation after deformation, while others rotate to a similar degree (or more) than those in the 200 °C annealed material. To further illustrate this rotation and streaking, the normalized intensity of the {111} diffraction ring is plotted as a function of azimuthal angle (ϕ) for each diffraction pattern in Fig. 11. The intensity of each azimuthal projection was normalized using the maximum value for ease of comparison. Using Gaussian peak fitting, we measure an average rotation of 7.75° for the as-deposited $Al_{85}Ni_{10}Ce_5$ and 5.6° for the annealed $Al_{85}Ni_{10}Ce_5$ due to the indentation. Using the first and last peaks in (Fig. 11, $\phi \approx 80^\circ - 90^\circ, 260^\circ - 270^\circ$), we measure an average peak broadening due to the deformation imposed by indentation of approximately 40° for the as-deposited sample, and negligible broadening ($< 3^\circ$) for the annealed $Al_{85}Ni_{10}Ce_5$, suggesting both a larger magnitude and broader distribution of grain rotation in the as-deposited $Al_{85}Ni_{10}Ce_5$.

Traditional DF images illuminating the regions where grain reorientation is most extreme are presented in Fig. 11. These images were collected by placing the objective aperture over the {111} and {200} diffraction rings near $\phi = 100^\circ - 140^\circ$, schematically shown in the inset in Fig. 12a. The placement of the objective aperture was chosen such that regions that had undergone the most grain rotation would be illuminated. The azimuthal region between 100°-140° is ideal for

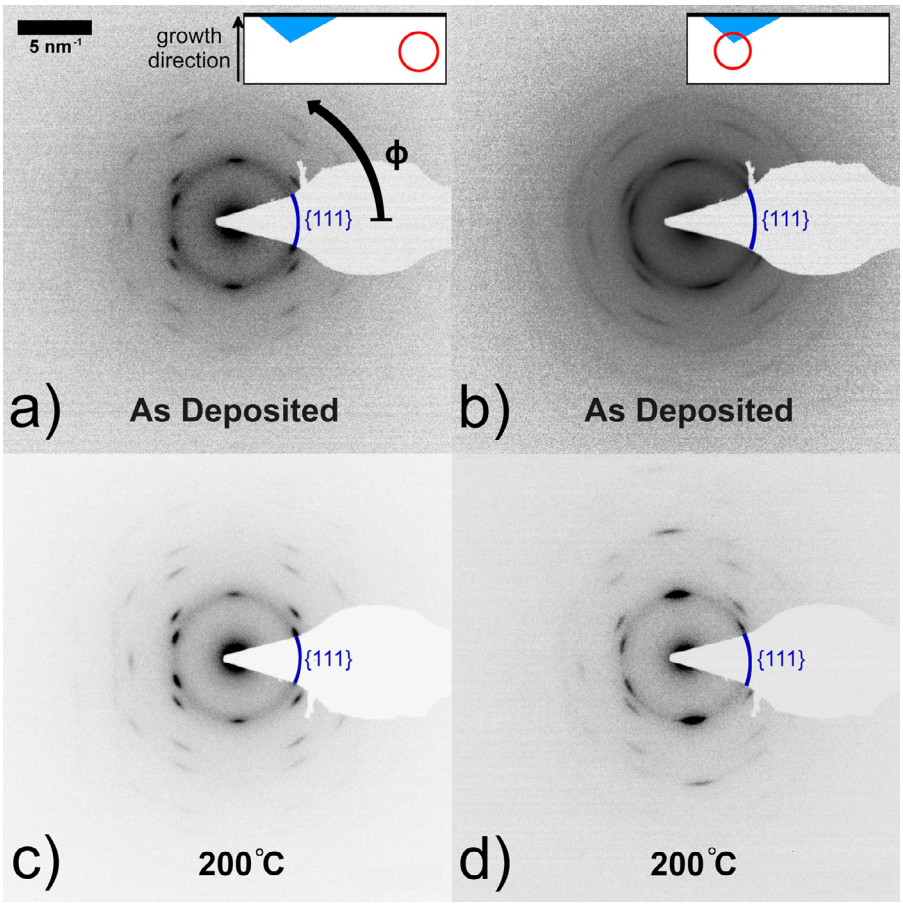

Fig. 10. Diffraction patterns taken from different selected area regions in the FIB prepared samples. (a,b) were taken from the as-deposited sample: (a) was taken away from the indent, (b) was taken from beneath the indent, schematically represented in the inset by the red circle. (c,d) were taken from the 200 °C sample: (c) away from the indent, (d) beneath the indent. The black arrow is used to indicate the origin and positive direction for the azimuthal projections in Fig. 11. (For interpretation of the references to colour in this figure legend, the reader is referred to the web version of this article.)

this analysis, as it does not include grains with the predominant undeformed texture. This can be seen in Fig. 11, where this region is between the two most prominent peaks for the intensities measured away from the indent. Fig. 12 illustrates that the largest degree of grain rotation is localized in small regions for both the as deposited (Fig. 12a) and 200 °C annealed samples. These regions correspond to the aforementioned dark regions in the bright field images (Figs. 9d, b). However, aside from the surface that deforms quite severely due to the contact with the indenter in both cases, the morphology of these regions beneath the contact surface differs dramatically between the two samples. Fig. 12a shows that the regions with the largest grain rotation extend nearly perpendicularly from the surface of the indent in the as-deposited material, whereas regions in the annealed material that exhibit the greatest degree of rotation (Fig. 12b) propagate vertically down from the surface of the indent. The details of this behavior will be discussed in detail in Section 5.2.

5. Discussion

Our results presented above indicate that the single-phase FCC nanocrystalline $Al_{85}Ni_{10}Ce_5$ prepared by sputter deposition exhibits a 7.6 nm average grain size, excellent mechanical properties (hardness $>$ 4.6 GPa) and good thermal stability (up to 0.7 T_m). Indentation experiments suggest that the hardness increases after annealing up to 325 °C while shear localization, as evinced by shear offsets in the pileup region of indentation experiments, is suppressed due to the formation of a Ni and Ce rich, amorphous grain boundary region. The objective of this discussion is to identify the mechanistic origins of this transition in deformation behavior.

5.1. Suppression of shear localization

The indent morphologies of the as-deposited $Al_{85}Ni_{10}Ce_5$ samples presented in Fig. 3a exhibit profuse shear band formation in the pileup region, a feature often observed during indentation of amorphous metals [81,82]. Vaidyanathan et al. [82] modeled the stress state around a Berkovich indentation using finite element simulations. They demonstrated that the circular pattern between corners of the Berkovich indenter corresponds to regions with the highest von Mises stress, thus the regions where shear band initiation would take place. This observation, in conjunction with existing macroscopic experiments on metallic glasses which demonstrate localized elastic-perfectly-plastic or shear softening behavior [83], explains why numerous shear offsets in such a circular pattern are often observed during indentation of metallic glasses. Nanocrystalline metals have similarly poor strain-hardening behavior and localized plasticity [84], but only rarely are such shear offsets observed. Several researchers [11,50,80,85] observed shear localization in the pileup region during indentation of nanocrystalline Ni-W with grain sizes $<$ 15 nm, concomitant with clear displacement bursts during loading, suggesting that the shear offsets are due to the discrete nature of plasticity in materials with such fine grain sizes.

Annealing the as-deposited $Al_{85}Ni_{10}Ce_5$ samples below 380 °C, prior to the onset of precipitation and coarsening, both increases the hardness dramatically (Fig. 5) and suppresses obvious shear

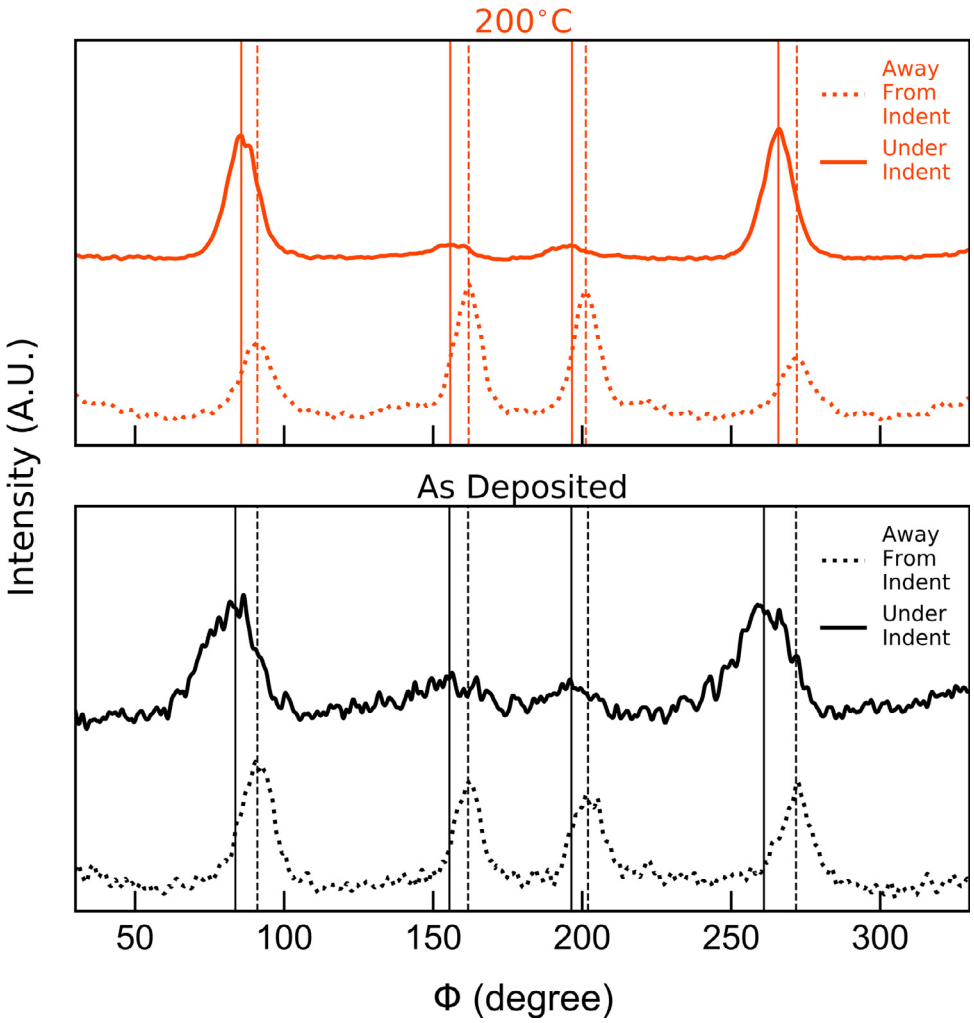

Fig. 11. Azimuthal projected intensities from the {111} diffraction ring from each of the FIB prepared samples. The intensities were normalized by their maximum and vertically offset for ease of interpretation. Vertical lines represent the peaks identified using a Gaussian peak fitting algorithm.

localization evident in the pileup region (Fig. 8, Section 4.3-4). This observation is markedly different from the behavior of nanocrystalline metals reported in the literature. Rupert et al. [50] performed annealing experiments on nanocrystalline Ni–W and observed similar magnitude increases in hardness due to annealing, but that the propensity for shear localization increased substantially. Additional pillar compression experiments suggest that this behavior occurs despite the activation of stress-assisted coarsening, which has been suggested to enhance plastic flow of nanocrystalline metals [41,42,64,80]. Several of these works [41,50] note that this increased propensity for shear localization due to annealing is quite similar to that of metallic glasses.

Processing routes can have a large impact on the shear localization behavior of metallic glasses. Most notably, nearly complete suppression of shear localization during indentation of metallic glasses has been observed for glasses driven to more rejuvenated, or liquid-like states [86–88]. Meng et al. [87] observed suppression of strong shear localization during indentation of a Zr-based metallic glass subjected to high pressure torsion (HPT). These authors report that the HPT process drives the structure of the material to a softer, more rejuvenated state, where there are many atomic sites where localized atomic rearrangements can occur. The more homogeneous distribution of these sites where atomic rearrangements can more easily occur manifests as a decrease in macroscopically observed shear localization. These authors (and others [86]) observe that the mechanical properties of the glass scale linearly with the degree of stored enthalpy where a harder glass exhibits a smaller stored enthalpy, implying a relaxed, lower energy state.

Annealing may relax non-equilibrium grain boundaries through the elimination of grain-boundary defects, limiting preferential sites where plasticity can initiate [41,50]. The argument follows that, similar to metallic glasses, nanocrystalline metals with a more uniform distribution of non-equilibrium boundaries may lead to a more homogeneous deformation morphology without obvious shear localization. However, while nanocrystalline metals with such a uniform distribution of non-equilibrium boundaries may deform more homogeneously, their deformation behavior is still undesirable. Such non-equilibrium boundaries are much more susceptible to deform via grain boundary sliding and atomic shuffling mechanisms, rather than dislocation-mediated plasticity (even those that interact strongly with grain boundaries). Grain boundary sliding and atomic shuffling are triggered at much lower levels of stress – suggesting a similar trade-off between strength and deformation morphology akin to that observed in metallic glasses. While this relationship – i.e. a more relaxed nanocrystalline metal is harder and is more prone to localization – has been observed in all previous studies [36,50,53,80], it is counter to what we observe in the nanocrystalline $Al_{85}Ni_{10}Ce_5$ (see Figs. 5 and 8). Brink and Albe [53] observed similar behavior to that observed in Ni–W alloys [41,50], where the degree of grain boundary relaxation is critical for predicting catastrophic shear localization in systems with a grain size $<$ 10 nm. They also suggest that the maximum strength of a nanocrystalline metal occurs when the grain

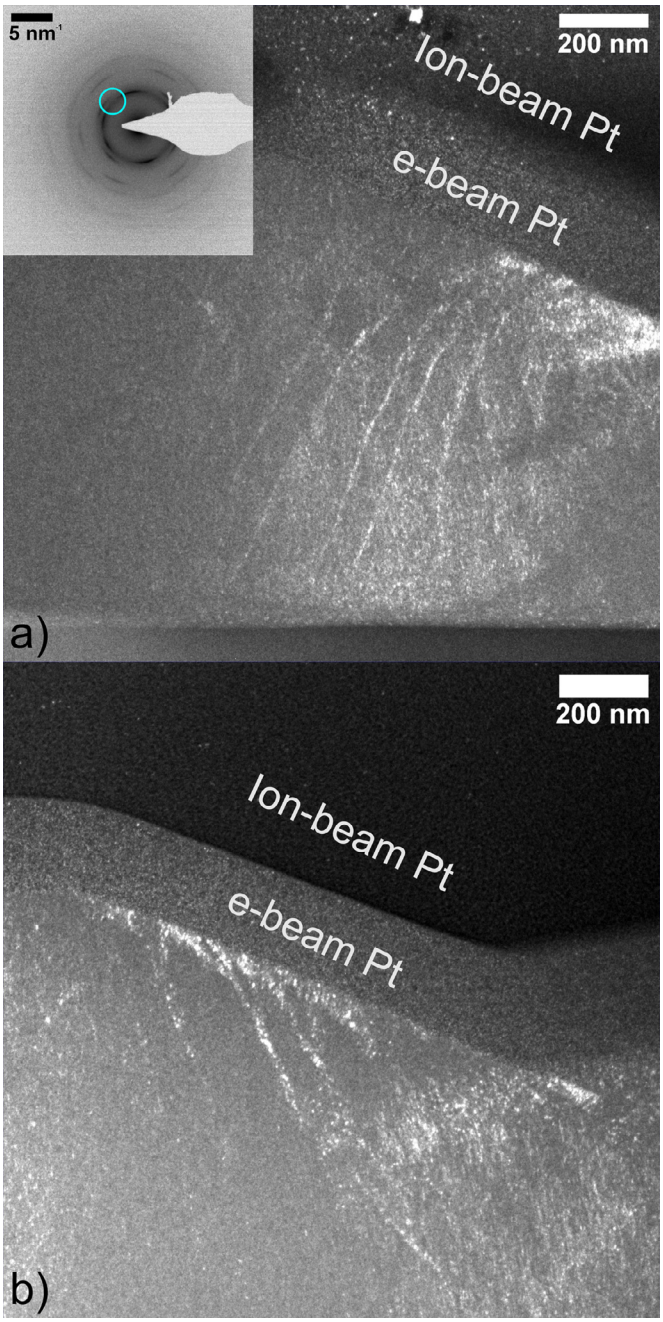

Fig. 12. DF TEM images from the (a) as-deposited and (b) 200 °C annealed sample. The objective aperture placement is shown schematically in the inset in (a) by the cyan circle, covering the {111} and {200} diffraction rings, in the regions between the peaks owing to the initial texture.

boundary state is well relaxed – the same condition where localization is most prominent. Again, our results suggest the opposite behavior: annealing the nanocrystalline $Al_{85}Ni_{10}Ce_5$ samples at low temperatures, presumably relaxing the material, not only induces increases in hardness and modulus, but the propensity for localization decreases, suggesting a fundamental difference between the $Al_{85}Ni_{10}Ce_5$ and materials investigated in previous studies.

5.2. Deformation mechanisms and texture

The strain rate sensitivity analysis presented in Fig. 6b, where no significant change in activation volume is observed due to annealing, allows us to conclude that grain boundary mediated deformation mechanisms are responsible for accommodating deformation in these alloys irrespective of the extent of chemical segregation. This is unsurprising given the microstructures presented in Fig. 4, which all exhibit a truly nanocrystalline microstructure despite annealing up to 0.7 T_m. There are numerous grain-boundary mediated deformation mechanisms operative in nanocrystalline metals, encompassing behavior ranging from atomic shuffling at grain boundaries [89], to grain rotation [5], sliding [13] and the slip of (partial) dislocations as they traverse grain interiors [90]. While many of these mechanisms are potentially deleterious due to their tendency for localization [12], many of the more exotic deformation mechanisms, such as sliding and rotation, can be suppressed through grain boundary relaxation and chemical segregation to grain boundaries, favoring predominantly dislocation-mediated plasticity [71,91–94]. Such a mechanistic transition is unlikely to manifest in strain rate sensitivity measurements, as these mechanisms are all expected to exhibit activation volumes in the range of $3-10b^3$ [73,95], which are difficult to isolate given the uncertainty of our measurements. However, subtle differences in deformation behavior are evident through textural analysis.

Detailed work from Lohmiller et al. [96] investigating the deformation of nanocrystalline Pd through in-situ synchrotron x-ray diffraction experiments concluded that grain boundary mediated deformation mechanisms, such as atomic shuffling and grain boundary shear and slip, do not cause the formation of a particular crystallographic texture. This is in contrast to dislocation-mediated mechanisms, which cause the formation of various crystallographic textures in both coarse grained FCC materials [97] and in highly segregated nanocrystalline metals [80,93]. Texture evolution in nanocrystalline metals has been broadly discussed by Weissmüller and Markmann [98] and others [99,100], who suggest that deformation accommodated by grain boundary mediated rotation and sliding may randomize pre-existing texture, whereas deformation accommodated by dislocation-mediated plasticity would favor crystallographic orientations where slip is easiest.

The diffraction patterns presented in Figs. 10 and 11, as well as the DF images in Fig. 12, suggest that the transition in deformation morphology observed in the $Al_{85}Ni_{10}Ce_5$ with annealing is due to a suppression of localized grain rotation and more homogenous dislocation-based plasticity. As mentioned in Section 4.4, when comparing Fig. 10c to Fig. 10d, it is evident that the majority of the grains in the annealed sample have undergone a rather uniform rotation of 5.6°, accommodating the imposed deformation without randomizing the texture. In the as-deposited condition (Figs. 10a and b), there is both significant grain rotation and randomization of the texture due to deformation. The initial texture formed during deposition favors {111} planes oriented with their normal along the growth direction, so the re-orientation of these grains to accommodate slip on $\{111\}\langle 1\bar{1}0\rangle$ directions is necessary for dislocation plasticity to participate in the deformation. The texture observed in the deformed material exhibits the same symmetry as the undeformed material with a 5.6° rotation. This is indicative of dislocation-mediated deformation [93,96,98–100] in the annealed $Al_{85}Ni_{10}Ce_5$, suggesting there is a mechanistic difference between the deformation of the as-deposited and annealed samples.

5.3. Evolution of deformation microstructure

The DF TEM images Fig. 12 highlight the differences due to annealing in the location of grains which undergo significant plasticity during indentation. While there is a great deal of plastic deformation at the surface in contact with the indenter, we focus our attention on the deformation occurring beneath the contact surface where we can more directly compare our observations to existing models of Berkovich indentation. Finite element modeling of Berkovich indentation has shown that during elastic loading, isostress contours of the resolved shear stress are oriented roughly normal to the

surface of the indent [101]. The DF image presented in Fig. 12a of the as-deposited material beneath the indent shows obvious grain rotation and localization in regions emanating in similar orientations (i.e. normal from the indent surface), suggesting that grains within these regions have rotated after reaching a critical flow stress. The corresponding diffraction pattern in Fig. 10b (and corresponding section of Fig. 11) exhibits delocalization and streaking of the peaks in the {111} diffraction ring. Due to the placement of the objective aperture (see inset in Fig. 12a), the grains that have given rise to the intensity in the image are those that have undergone the most significant rotation, specifically those responsible for the streaking of the secondary peak in Fig. 11 ($\phi = 150^{\circ} - 180^{\circ}$). Furthermore, according to the modeling work of Min et al. [102] the regions that exhibit severe grain rotation in the as-deposited $Al_{85}Ni_{10}Ce_5$ extend past contours of appreciable plastic strain predicted by the model. The excellent agreement of the spatial pattern of grain rotation with isostress contours [101], rather than plastic strain contours [102], suggests that the deformation in the as-deposited $Al_{85}Ni_{10}Ce_5$ is primarily facilitated by grain boundary mediated deformation mechanisms such as atomic shuffling, grain rotation, and sliding, rather than dislocation-mediated deformation, ultimately leading to softening and strain localization after initiation at a critical stress.

Iso-contours of accumulated plastic strain from finite element modeling [102] agree quite well with the illuminated regions in the annealed $Al_{85}Ni_{10}Ce_5$ (Fig. 12b). In the annealed $Al_{85}Ni_{10}Ce_5$, grain rotation is most prominent in regions with the largest accumulated plastic strain, further suggesting that the annealed sample exhibits predominantly dislocation based plasticity. This preference for dislocation based plasticity over non-dislocation based grain boundary mediated deformation mechanisms gives rise to the transition in deformation morphology from strong localization in the as-deposited state to homogeneous deformation in the annealed condition. However, a key question remains: why does the segregation of Ni and Ce to grain boundaries and the formation of an amorphous intergranular region induce a transition from grain boundary-mediated to dislocation-mediated deformation and suppress shear localization?

5.4. Enhanced mechanical properties of nanocrystalline Al–Ni–Ce

To better understand the role of the Ni and Ce rich grain boundary, we turn our focus to the mechanical properties of the $Al_{85}Ni_{10}Ce_5$ samples which exhibit ultrahigh hardness. The mechanical behavior of rapidly solidified amorphous Al-Ni-Ce alloys with similar compositions reported by Inoue et al. [55,57] exhibit hardness values ranging from 2.6 to 4.7 GPa subject to various annealing procedures. The materials explored in that study with highest hardness are generally brittle and contain a large density of both crystalline Al and intermetallic phases [55]. The mechanical behavior of other binary nanocrystalline Al based alloys have been reported in the literature, but hardness measurements exceeding 2 GPa are mainly observed in alloys with two-phase microstructures with a large density of brittle intermetallic compounds [103]. Recently, nanocrystalline Al–Mg alloys have been prepared using mechanical alloying that exhibit hardness values exceeding 4.5 GPa after annealing due to strong grain boundary segregation [94]. Thus, the high hardness of the as deposited $Al_{85}Ni_{10}Ce_5$ of 4.67 ± 0.24 GPa is quite remarkable, and the exceptionally high hardness of 5.62 ± 0.41 GPa in the 325 °C annealed condition stands apart from other Al alloys (Fig. 4).

A traditional Hall-Petch [104,105] analysis is insufficient for predicting the mechanical behavior of the as-deposited Al_{85} $Ni_{10}Ce_5$ due to the small grain size and complex chemical environment at the grain boundaries. Utilizing Hall–Petch coefficients from [106], the grain size reported in Fig. 1, a Tabor factor of 3 [107], and even including a term for solid solution strengthening [108], we calculate an expected hardness of 1.55 GPa, significantly lower than what is measured. Thus, the remainder of the hardening must be linked to the role of grain boundary chemistry in mediating dislocations nucleation and propagation.

The change in mechanical response due to the formation of a Ni and Ce rich amorphous intergranular film formed during annealing can be reconciled by the elastic contrast between the grain interior and the grain boundary. From the existing studies of Al–Ni–Ce amorphous alloys [56], along with the HAADF images in Fig. 4, it is clear that annealing drives strong chemical segregation of Ni and Ce to the grain boundaries. This is expected to energetically relax the grain boundaries as well as mechanically stiffen them, making them less prone to sliding or localized atomic shuffling [8,91,92]. Simulations of grain boundaries in nominally pure systems have demonstrated that grain boundaries themselves exhibit lower moduli than their crystalline counterparts [109,110]. The small increase in modulus in Fig. 5 at temperatures below 0.7 T_m is indicative of such a segregation/relaxation induced stiffening of the grain boundaries. Furthermore, grain boundary stiffness has been shown to substantially affect the behavior of intragranular dislocations [111]. Fundamentally, this can be understood from an image force perspective, where an elastically stiff, Ni and Ce rich extended grain boundary would exert a repulsive force on any intragranular dislocations, in addition to providing strong dislocation pinning.

In order to understand the enhancement in mechanical properties due to the formation and evolution of the spatially extended, amorphous grain boundary (Fig. 13a), we propose the following model, shown schematically in Fig. 13b. Using the grain boundary widths measured in Fig. 7 and assuming cuboidal grains with an average grain size of that presented in Fig. 1, we estimate a volume fraction of grain boundary content in the samples of approximately 36%. Using this volume fraction, in combination with the moduli measured experimentally using indentation (Fig. 5), we can estimate the modulus evolution of the grain boundary region. Assuming that the modulus is partitioned such that that the grain interiors upon annealing are pure Al with a Young's modulus of 69 GPa [112], and can be described using a Voigt-type rule of mixtures [113], we estimate grain boundary moduli of approximately 200 GPa for the annealed samples. This estimated modulus is high due to the extremely low modulus of the grain interiors, but is quite similar to that of pure Ni [114], thus we view this as an upper bound for the stiffness of the grain boundary. Using the image force analysis of Öveçolu et al. [115], we can calculate the force on a screw dislocation within the Al grain as a function of distance from the neighboring Ni–Ce rich grain boundaries (shown schematically with an edge dislocation in Fig. 13b). This model suggests that there is an equilibrium distance of a dislocation several burgers vectors from the adjacent Ni/Ce layers (3.4 b for the 200 °C sample and 3.9 b for the 325 °C sample), and a rapidly increasing repulsive force for a dislocation closer to the adjacent layers. The image force construction breaks down when the distance of the screw dislocation to the interface is very small. Therefore, to estimate the maximum repulsive force on the dislocation, we choose a distance of 1.5 b away from the interface to calculate the maximum resistance for dislocation propagation. The repulsive force on a dislocation at a distance of 1.5 b from the interface, normalized by the image force $f = \frac{\mu b^2}{2\pi D}$, where μ is the shear modulus, D is the average grain size, and b is the burgers vector, is 1.99 in the 200 °C sample and 2.43 for the 325 °C sample. The corresponding far field stress required to overcome this barrier is 296 MPa and 362 MPa for the 200 °C and 362 MPa annealed samples, respectively. Incorporating this increased resistance to dislocation motion due to the spatially extended, stiffer grain boundary region, we predict that the increase in hardness is $\Delta H = 3 * \Delta\sigma_y$ of 888 MPa for 200 °C or 1.08 GPa for 325 °C. The measured changes in hardness for these samples compared to the as-deposited material are 820 MPa (200 °C) and 950 MPa (325 °C), which are in excellent agreement with the model prediction. Schematically, the effects of the amorphous intergranular film are shown in Fig. 13c, where a dislocation

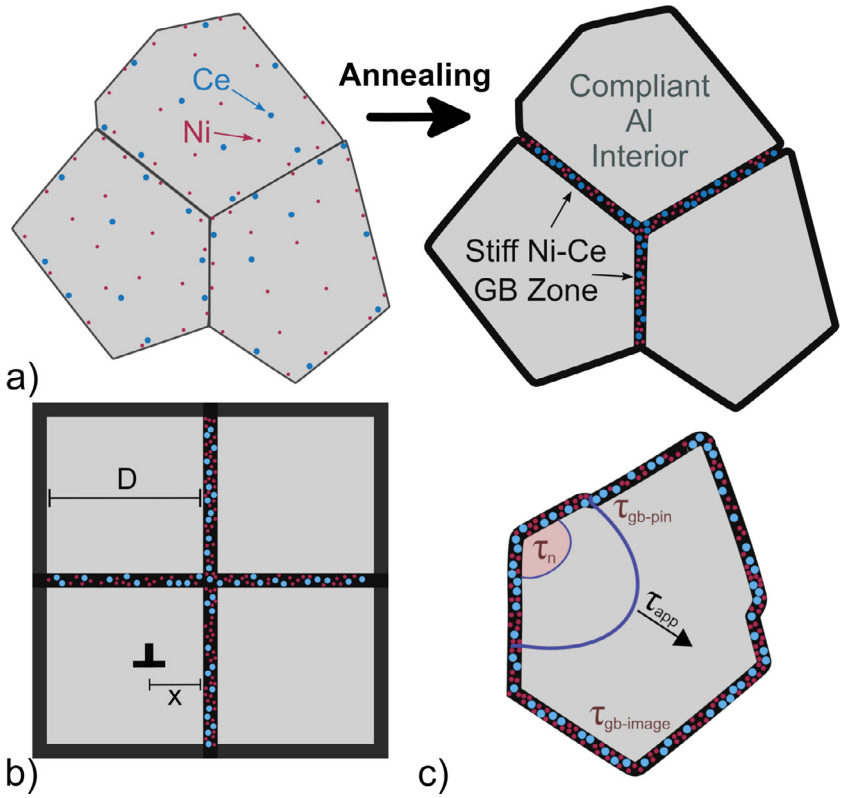

Fig. 13. Schematic demonstrating (a) the formation of a Ni and Ce rich amorphous grain boundary during annealing, (b) the model proposed in Section 5.4 with a dislocation embedded in an Al grain of length D and distance X from the grain boundary, and (c) the ability of the annealed $Al_{85}Ni_{10}Ce_5$ to accommodate dislocations at the amorphous grain boundaries without transmitting or nucleating new dislocations in neighboring grains.

traversing the grain must overcome the barrier for nucleation (τ_n), the barrier due to pinning forces at the grain boundary (τ_{pin}), as well as the image forces from the stiff grain boundary region (τ_{gb}) in order to move under the applied stress (τ).

The image force analysis above suggests that the formation of a stiff, amorphous intergranular film, in contrast with a compliant grain interior rationalizes the enhanced hardness of the annealed $Al_{85}Ni_{10}Ce_5$. Additional implications on the mechanical response due to the presence of an amorphous intergranular film include the suppression of shear localization. Pan and Rupert [44] simulated dislocation-grain-boundary interactions in Cu–Zr with amorphous grain boundaries, and observed that the presence of an amorphous grain boundary enables the absorption of several dislocations prior to failure. The simulations also indicate that the von Mises stress in neighboring grains is nearly unaffected by the absorption of dislocations at the amorphous grain boundary, whereas the absorption of a dislocation at an atomically sharp grain boundary leads to high stresses and crack formation. Given this behavior in simulations, the formation of a Ni–Ce rich amorphous intergranular film may be responsible for the suppression of long-range localization. In conjunction with the suppression of grain-boundary mediated mechanisms in favor of dislocation-mediated plasticity, the tendency for a grain boundary to absorb several dislocations prior to initiating plasticity in neighboring grains would prevent the formation of a percolating path necessary for localization. Pan and Rupert [44] demonstrated that for a 1 nm thick amorphous grain boundary, at least two dislocations can be accommodated prior to crack formation. Given the large shear strain induced by a single dislocation traversing a 7.6 nm grain ($b/D \approx 4.63\%$ [96]) for the $Al_{85}Ni_{10}Ce_5$, it is possible for the amorphous grain boundaries present in the annealed $Al_{85}Ni_{10}Ce_5$ to accommodate the deformation without affecting neighboring grains. Furthermore, despite the thickness of the amorphous grain boundaries present in the $Al_{85}Ni_{10}Ce_5$ remaining relatively constant due to annealing above 200 °C (Fig. 7), the segregation-driven increase in stiffness of the grain boundary likely provides additional screening of dislocations that impinge on the grain boundaries [111]. Such screening would further inhibit long range localization, promoting both high strength and homogeneous plastic flow. Thus, the role of such a stiff Ni–Ce rich amorphous intergranular film serves three primary purposes: (1) to impede the intragranular motion of a dislocation providing increased strength, (2) to serve as a strong obstacle for intergranular dislocation transmission, and (3) to provide additional accommodation of impinging dislocations at the grain boundary, all of which assist in mitigating the propensity for localization.

6. Conclusions

In this work we have investigated the mechanical behavior of a FCC nanocrystalline Al–Ni–Ce alloy prepared by sputter deposition followed by systematic annealing to drive segregation to grain boundaries. The detailed indentation analysis and electron microscopy investigations of the deformed material allow us to draw the following conclusions:

- The $Al_{85}Ni_{10}Ce_5$ sample exhibits many desirable properties, such as a very small grain size (7.6 nm), high hardness (exceeding 4.6 GPa) and thermal stability (up to 0.7 T_m).
- Investigations of the indentation morphologies indicate that shear localization, as evinced by shear offsets in the pileup region of indentation experiments, is prominent in the as-deposited state and suppressed due to low temperature annealing.
- TEM analysis of the as deposited and 200 °C annealed material indicate that the degree of grain rotation, as well as the spatial distribution of regions that have undergone significant plasticity, are different, despite identical loading conditions during indentation.

- This transition in grain rotation behavior and suppression of obvious shear localization coincides with the formation of amorphous content in the material, likely in the form of an amorphous intergranular film.
- Image force analysis indicates that the presence of such a stiff intergranular film in contrast with a compliant grain interior is responsible for the increases in strength observed during low temperature annealing, as well as preventing long range localization by promoting uniform dislocation-based plasticity over grain-boundary mediated deformation processes.

This work suggests that the relationship between mechanical behavior, including strength, propensity for shear localization, and deformation morphology in nanocrystalline alloys may be more complex than the literature would suggest. Specifically, understanding the intricacies of grain boundaries are crucial for predicting the behavior of interface-dominated materials such as nanocrystalline metals. The specific alloy studied here exhibits attractive properties that are worthy of future detailed study, and alloying strategies presented in this work may enable the design of nanocrystalline metals with greater functionality than current alloys.

Acknowledgment

This work was funded by NSF CMMI-1724519. GHB was supported by a NSF GRFP Award No. 1650114. The authors would like to thank Dr. Verena Maier-Kiener for helpful discussions about indentation analysis, Dr. Aidan Taylor and Dr. Claire Chisholm for their microscopy assistance, and Deryck Stave for assistance during sputter deposition. The MRL Shared Experimental Facilities are supported by the MRSEC Program of the NSF under Award No. DMR 1720256; a member of the NSF-funded Materials Research Facilities Network (www.mrfn.org).

References

[1] K. Kumar, H. Van Swygenhoven, S. Suresh, Mechanical behavior of nanocrystalline metals and alloys, Acta Mater. 51 (19) (2003) 5743–5774, doi: 10.1016/J.ACTAMAT.2003.08.032.
[2] B.L. Boyce, H.A. Padilla, Anomalous fatigue behavior and fatigue-Induced grain growth in nanocrystalline nickel alloys, Metall. Mater. Trans. A 42 (7) (2011) 1793–1804, doi: 10.1007/s11661-011-0708-x.
[3] J.F. Curry, T.F. Babuska, T.A. Furnish, P. Lu, D.P. Adams, A.B. Kustas, B.L. Nation, M.T. Dugger, M. Chandross, B.G. Clark, B.L. Boyce, C.A. Schuh, N. Argibay, Achieving ultralow wear with stable nanocrystalline metals, Adv. Mater. 30 (32) (2018) 1802026, doi: 10.1002/adma.201802026.
[4] T.J. Rupert, C.A. Schuh, Sliding wear of nanocrystalline Ni-W: structural evolution and the apparent breakdown of archard scaling, Acta Mater. 58 (12) (2010) 4137–4148, doi: 10.1016/J.ACTAMAT.2010.04.005.
[5] Z. Shan, E.A. Stach, J.M.K. Wiezorek, J.A. Knapp, D.M. Follstaedt, S.X. Mao, Grain boundary-mediated plasticity in nanocrystalline nickel., Science 305 (5684) (2004) 654–657, doi: 10.1126/science.1098741.
[6] T.J. Rupert, J.C. Trenkle, C.A. Schuh, Enhanced solid solution effects on the strength of nanocrystalline alloys, Acta Mater. 59 (4) (2011) 1619–1631, doi: 10.1016/j.actamat.2010.11.026.
[7] J. Hu, Y.N. Shi, X. Sauvage, G. Sha, K. Lu, Grain boundary stability governs hardening and softening in extremely fine nanograined metals., Science 355 (6331) (2017) 1292–1296, doi: 10.1126/science.aal5166.
[8] L. Zhang, C. Lu, Y. Shibuta, Shear response of grain boundaries with metastable structures by molecular dynamics simulations, Modell. Simul. Mater. Sci. Eng. 26 (3) (2018) 035008, doi: 10.1088/1361-651X/aaacaa.
[9] M. Meyers, A. Mishra, D. Benson, Mechanical properties of nanocrystalline materials, Prog. Mater. Sci. 51 (4) (2006) 427–556, doi: 10.1016/J.PMATSCI.2005.08.003.
[10] Q. Wei, D. Jia, K.T. Ramesh, E. Ma, Evolution and microstructure of shear bands in nanostructured fe, Appl. Phys. Lett. 81 (7) (2002) 1240–1242, doi: 10.1063/1.1501158.
[11] J.R. Trelewicz, C.A. Schuh, The hall-Petch breakdown in nanocrystalline metals: a crossover to glass-like deformation, Acta Mater. 55 (17) (2007) 5948–5958, doi: 10.1016/J.ACTAMAT.2007.07.020.
[12] T.J. Rupert, Strain localization in a nanocrystalline metal: atomic mechanisms and the effect of testing conditions, J. Appl. Phys. 114 (3) (2013) 033527, doi: 10.1063/1.4815965.
[13] H. Van Swygenhoven, P.M. Derlet, Grain-boundary sliding in nanocrystalline fcc metals, Phys. Rev. B 64 (22) (2001) 224105, doi: 10.1103/PhysRevB.64.224105.
[14] R. Birringer, Nanocrystalline materials, Mater. Sci. Eng.: A 117 (1989) 33–43, doi: 10.1016/0921-5093(89)90083-X.
[15] J. Weissmüller, W. Krauss, T. Haubold, R. Birringer, H. Gleiter, Atomic structure and thermal stability of nanostructured Y-Fe alloys, Nanostruct. Mater. 1 (6) (1992) 439–447, doi: 10.1016/0965-9773(92)90076-A.
[16] J. Weissmüller, Alloy effects in nanostructures, Nanostruct. Mater. 3 (1–6) (1993) 261–272, doi: 10.1016/0965-9773(93)90088-S.
[17] A. Tschöpe, R. Birringer, Thermodynamics of nanocrystalline platinum, Acta Metall. Mater. 41 (9) (1993) 2791–2796, doi: 10.1016/0956-7151(93)90147-K.
[18] J. Löffler, J. Weissmüller, Grain-boundary atomic structure in nanocrystalline palladium from x-ray atomic distribution functions, Phys. Rev. B 52 (10) (1995) 7076–7093, doi: 10.1103/PhysRevB.52.7076.
[19] C.E. Krill III, R. Klein, S. Janes, R. Birringer, Thermodynamic stabilization of grain boundaries in nanocrystalline alloys, Mater. Sci. Forum 179–181 (1995) 443–448, doi: 10.4028/www.scientific.net/MSF.179–181.443.
[20] J. Weissmüller, Thermodynamics of nanocrystalline solids. In *Nanocrystalline Metals and Oxides*, Springer, Boston, MA, 2002, pp. 1–39.
[21] R. Kirchheim, Grain coarsening inhibited by solute segregation, Acta Mater. 50 (2) (2002) 413–419, doi: 10.1016/S1359-6454(01)00338-X.
[22] F. Liu, R. Kirchheim, Grain boundary saturation and grain growth, Scr. Mater. 51 (6) (2004) 521–525, doi: 10.1016/j.scriptamat.2004.05.042.
[23] C.E. Krill, H. Ehrhardt, R. Birringer, Thermodynamic stabilization of nanocrystallinity, Z. Metall. 96 (10) (2005) 1134–1141, doi: 10.3139/146.101152.
[24] R. KIRCHHEIM, Reducing grain boundary, dislocation line and vacancy formation energies by solute segregation. I. Theoretical background, Acta Mater. 55 (15) (2007) 5129–5138, doi: 10.1016/j.actamat.2007.05.047.
[25] R. KIRCHHEIM, Reducing grain boundary, dislocation line and vacancy formation energies by solute segregation II. Experimental evidence and consequences, Acta Mater. 55 (15) (2007) 5139–5148, doi: 10.1016/j.actamat.2007.05.033.
[26] T. Chookajorn, H.A. Murdoch, C.A. Schuh, Design of stable nanocrystalline alloys, Science 337 (6097) (2012) 951–954, doi: 10.1126/science.1224737.
[27] H.A. Murdoch, C.A. Schuh, Stability of binary nanocrystalline alloys against grain growth and phase separation, Acta Mater. 61 (6) (2013) 2121–2132, doi: 10.1016/J.ACTAMAT.2012.12.033.
[28] N. Vo, J. Schäfer, R. Averback, K. Albe, Y. Ashkenazy, P. Bellon, Reaching theoretical strengths in nanocrystalline Cu by grain boundary doping, Scr. Mater. 65 (8) (2011) 660–663, doi: 10.1016/J.SCRIPTAMAT.2011.06.048.
[29] S. Özerinç, K. Tai, N.Q. Vo, P. Bellon, R.S. Averback, W.P. King, Grain boundary doping strengthens nanocrystalline copper alloys, Scr. Mater. 67 (7–8) (2012) 720–723, doi: 10.1016/J.SCRIPTAMAT.2012.06.031.
[30] T. Frolov, K. Darling, L. Kecskes, Y. Mishin, Stabilization and strengthening of nanocrystalline copper by alloying with tantalum, Acta Mater. 60 (5) (2012) 2158–2168, doi: 10.1016/J.ACTAMAT.2012.01.011.
[31] G. Gottstein, D.A. Molodov, L.S. Shvindlerman, Grain boundary migration in metals: recent developments, Interface Sci. 6 (1/2) (1998) 7–22, doi: 10.1023/A:1008641617937.
[32] A. Detor, C. Schuh, Microstructural evolution during the heat treatment of nanocrystalline alloys, J. Mater. Res. 22 (11) (2007) 3233–3248, doi: 10.1557/JMR.2007.0403.
[33] M.-R. He, P.J. Felfer, S. Dasgupta, S.K. Samudrala, P.J. Malone, G. Feng, K.J. Hemker, J.M. Cairney, D.S. Gianola, Understanding the mechanical behavior of nanocrystalline Al-O thin films with complex microstructures, Acta Mater. 77 (2014) 269–283, doi: 10.1016/J.ACTAMAT.2014.05.058.
[34] Z. Huang, F. Chen, Q. Shen, L. Zhang, T.J. Rupert, Combined effects of nonmetallic impurities and planned metallic dopants on grain boundary energy and strength, Acta Mater. 166 (2019) 113–125, doi: 10.1016/j.actamat.2018.12.031.
[35] C. Carlton, P. Ferreira, What is behind the inverse Hall-Petch effect in nanocrystalline materials? Acta Mater. 55 (11) (2007) 3749–3756, doi: 10.1016/J.ACTAMAT.2007.02.021.
[36] A. Khalajhedayati, T.J. Rupert, Emergence of localized plasticity and failure through shear banding during microcompression of a nanocrystalline alloy, Acta Mater. 65 (2014) 326–337, doi: 10.1016/J.ACTAMAT.2013.10.074.
[37] P. Hua, K. Chu, Q. Sun, Grain refinement and amorphization in nanocrystalline NiTi micropillars under uniaxial compression, Scr. Mater. 154 (2018) 123–126, doi: 10.1016/J.SCRIPTAMAT.2018.05.034.
[38] G. He, J. Eckert, W. Löser, L. Schultz, Novel Ti-base nanostructure-dendrite composite with enhanced plasticity, Nat. Mater. 2 (1) (2003) 33–37, doi: 10.1038/nmat792.
[39] T. Frolov, D.L. Olmsted, M. Asta, Y. Mishin, Structural phase transformations in metallic grain boundaries, Nat. Commun. 4 (1) (2013) 1899, doi: 10.1038/ncomms2919.
[40] D.B. Bober, M. Kumar, T.J. Rupert, Nanocrystalline grain boundary engineering: increasing $\Sigma 3$ boundary fraction in pure Ni with thermomechanical treatments, Acta Mater. 86 (2015) 43–54, doi: 10.1016/J.ACTAMAT.2014.11.034.
[41] A. Khalajhedayati, T.J. Rupert, High-temperature stability and grain boundary complexion formation in a nanocrystalline Cu-Zr alloy, JOM 67 (12) (2015) 2788–2801, doi: 10.1007/s11837-015-1644-9.
[42] A. Khalajhedayati, Z. Pan, T.J. Rupert, Manipulating the interfacial structure of nanomaterials to achieve a unique combination of strength and ductility, Nat. Commun. 7 (2016) 10802, doi: 10.1038/ncomms10802.
[43] Z. Pan, T.J. Rupert, Damage nucleation from repeated dislocation absorption at a grain boundary, Comput. Mater. Sci 93 (2014) 206–209, doi: 10.1016/J.COMMATSCI.2014.07.008.
[44] Z. Pan, T.J. Rupert, Amorphous intergranular films as toughening structural features, Acta Mater. 89 (2015) 205–214, doi: 10.1016/j.actamat.2015.02.012.

[45] V. Turlo, T.J. Rupert, Grain boundary complexions and the strength of nanocrystalline metals: dislocation emission and propagation, Acta Mater. 151 (2018) 100–111, doi: 10.1016/j.actamat.2018.03.055.
[46] J.D. Schuler, T.J. Rupert, Materials selection rules for amorphous complexion formation in binary metallic alloys, Acta Mater. 140 (2017) 196–205, doi: 10.1016/J.ACTAMAT.2017.08.042.
[47] A. Inoue, Stabilization of metallic supercooled liquid and bulk amorphous alloys, Acta Mater. 48 (1) (2000) 279–306, doi: 10.1016/S1359-6454(99)00300-6.
[48] J. Han, V. Vitek, D.J. Srolovitz, Grain-boundary metastability and its statistical properties, Acta Mater. 104 (2016) 259–273, doi: 10.1016/J.ACTAMAT.2015.11.035.
[49] J. Han, S.L. Thomas, D.J. Srolovitz, Grain-boundary kinetics: a unified approach, Prog. Mater. Sci. 98 (2018) 386–476, doi: 10.1016/J.PMATSCI.2018.05.004.
[50] T.J. Rupert, J.R. Trelewicz, C.A. Schuh, Grain boundary relaxation strengthening of nanocrystalline Ni-W alloys, J. Mater. Res. 27 (9) (2012) 1285–1294, doi: 10.1557/jmr.2012.55.
[51] O. Renk, A. Hohenwarter, K. Eder, K. Kormout, J. Cairney, R. Pippan, Increasing the strength of nanocrystalline steels by annealing: is segregation necessary? Scr. Mater. 95 (2015) 27–30, doi: 10.1016/J.SCRIPTAMAT.2014.09.023.
[52] G.H. Balbus, M.P. Echlin, C.M. Grigorian, T.J. Rupert, T.M. Pollock, D.S. Gianola, Femtosecond laser rejuvenation of nanocrystalline metals, Acta Mater. 156 (2018) 183–195, doi: 10.1016/J.ACTAMAT.2018.06.027.
[53] T. Brink, K. Albe, From metallic glasses to nanocrystals: molecular dynamics simulations on the crossover from glass-like to grain-boundary-mediated deformation behaviour, Acta Mater. 156 (2018) 205–214, doi: 10.1016/J.ACTAMAT.2018.06.036.
[54] A. Inoue, K. Ohtera, T. Masumoto, New amorphous Al-Y, Al-La and Al-Ce alloys prepared by melt spinning, Jpn. J. Appl. Phys. 27 (Part 2, No. 5) (1988) L736–L739, doi: 10.1143/JJAP.27.L736.
[55] A. Inoue, K. Nakazato, Y. Kawamura, T. Masumoto, The effect of Cu addition on the structure and mechanical properties of Al-Ni-M (M - Ce or Nd) amorphous alloys containing nanoscale f.c.c.-Al particles, Mater. Sci. Eng.: A 179–180 (1994) 654–658, doi: 10.1016/0921-5093(94)90287-9.
[56] K. Hono, Y. Zhang, A. Tsai, A. Inoue, T. Sakurai, Solute partitioning in partially crystallized Al-Ni-Ce(-Cu) metallic glasses, Scr. Metall. Mater. 32 (2) (1995) 191–196, doi: 10.1016/S0956-716X(99)80035-1.
[57] A. Inoue, H. Kimura, Fabrications and mechanical properties of bulk amorphous, nanocrystalline, nanoquasicrystalline alloys in aluminum-based system, J. Light Met. 1 (1) (2001) 31–41, doi: 10.1016/S1471-5317(00)00004-3.
[58] T. Akopyan, N. Belov, E. Naumova, N. Letyagin, New in-situ Al matrix composites based on Al-Ni-La eutectic, Mater. Lett. 245 (2019) 110–113, doi: 10.1016/J.MATLET.2019.02.112.
[59] J. Guo, K. Ohtera, Microstructures and mechanical properties of rapidly solidified high strength Al-Ni based alloys, Acta Mater. 46 (11) (1998) 3829–3838, doi: 10.1016/S1359-6454(98)00065-2.
[60] A. Plotkowski, O. Rios, N. Sridharan, Z. Sims, K. Unocic, R. Ott, R. Dehoff, S. Babu, Evaluation of an Al-Ce alloy for laser additive manufacturing, Acta Mater. 126 (2017) 507–519, doi: 10.1016/J.ACTAMAT.2016.12.065.
[61] H. Wang, Z. Li, Z. Chen, B. Yang, Thermodynamic optimization of the Ni-Al-Ce ternary system, J. Phase Equilib. Diffus. 37 (2) (2016) 222–228, doi: 10.1007/s11669-015-0447-6.
[62] A. Tsai, T. Kamiyama, Y. Kawamura, A. Inoue, T. Masumoto, Formation and precipitation mechanism of nanoscale al particles in Al-Ni base amorphous alloys, Acta Mater. 45 (4) (1997) 1477–1487, doi: 10.1016/S1359-6454(96)00268-6.
[63] G. Waterloo, H. Jones, Microstructure and thermal stability of melt-spun Al-Nd and Al-Ce alloy ribbons, J. Mater. Sci. 31 (9) (1996) 2301–2310, doi: 10.1007/BF01152938.
[64] D. Gianola, S. Van Petegem, M. Legros, S. Brandstetter, H. Van Swygenhoven, K. Hemker, Stress-assisted discontinuous grain growth and its effect on the deformation behavior of nanocrystalline aluminum thin films, Acta Mater. 54 (8) (2006) 2253–2263, doi: 10.1016/J.ACTAMAT.2006.01.023.
[65] A. Kobler, J. Lohmiller, J. Schäfer, M. Kerber, A. Castrup, A. Kashiwar, P.A. Gruber, K. Albe, H. Hahn, C. Kübel, Deformation-induced grain growth and twinning in nanocrystalline palladium thin films, Beilstein J. Nanotechnol. 4 (2013) 554–566, doi: 10.3762/bjnano.4.64.
[66] A. Castrup, C. Kübel, T. Scherer, H. Hahn, Microstructure and residual stress of magnetron sputtered nanocrystalline palladium and palladium gold films on polymer substrates, J. Vac Sci. Technol. A: Vac Surf. Films 29 (2) (2011) 021013, doi: 10.1116/1.3554265.
[67] W. Oliver, G. Pharr, An improved technique for determining hardness and elastic modulus using load and displacement sensing indentation experiments, J. Mater. Res. 7 (06) (1992) 1564–1583, doi: 10.1557/JMR.1992.1564.
[68] M. Ohring, Materials Science of Thin Films: Deposition and Structure, Academic Press, 2002.
[69] G. Wu, C. Liu, L. Sun, Q. Wang, B. Sun, B. Han, J.J. Kai, J. Luan, C.T. Liu, K. Cao, Y. Lu, L. Cheng, J. Lu, Hierarchical nanostructured aluminum alloy with ultrahigh strength and large plasticity, Nat. Commun. 10 (1) (2019), doi: 10.1038/s41467-019-13087-4.
[70] G. Kim, X. Chai, L. Yu, X. Cheng, D.S. Gianola, Interplay between grain boundary segregation and electrical resistivity in dilute nanocrystalline Cu alloys, Scr. Mater. 123 (2016) 113–117, doi: 10.1016/J.SCRIPTAMAT.2016.06.008.
[71] M.-R. He, S.K. Samudrala, G. Kim, P.J. Felfer, A.J. Breen, J.M. Cairney, D.S. Gianola, Linking stress-driven microstructural evolution in nanocrystalline aluminium with grain boundary doping of oxygen, Nat. Commun. 7 (2016) 11225, doi: 10.1038/ncomms11225.
[72] T.Y. Tsui, W.C. Oliver, G.M. Pharr, Influences of stress on the measurement of mechanical properties using nanoindentation: part I. Experimental studies in an aluminum alloy, J. Mater. Res. 11 (3) (1996) 752–759, doi: 10.1557/JMR.1996.0091.
[73] V. Maier, K. Durst, J. Mueller, B. Backes, H.W. Höppel, M. Göken, Nanoindentation strain-rate jump tests for determining the local strain-rate sensitivity in nanocrystalline ni and ultrafine-grained al, J. Mater. Res. 26 (11) (2011) 1421–1430, doi: 10.1557/jmr.2011.156.
[74] V. Maier, B. Merle, M. Göken, K. Durst, An improved long-term nanoindentation creep testing approach for studying the local deformation processes in nanocrystalline metals at room and elevated temperatures, J. Mater. Res. 28 (9) (2013) 1177–1188, doi: 10.1557/jmr.2013.39.
[75] O. Renk, V. Maier-Kiener, I. Issa, J. Li, D. Kiener, R. Pippan, Anneal hardening and elevated temperature strain rate sensitivity of nanostructured metals: their relation to intergranular dislocation accommodation, Acta Mater. 165 (2019) 409–419, doi: 10.1016/j.actamat.2018.12.002.
[76] J.R. Trelewicz, C.A. Schuh, Grain boundary segregation and thermodynamically stable binary nanocrystalline alloys, Phys. Rev. B 79 (9) (2009) 094112, doi: 10.1103/PhysRevB.79.094112.
[77] S.J. Dillon, M. Tang, W.C. Carter, M.P. Harmer, Complexion: a new concept for kinetic engineering in materials science, Acta Mater. 55 (18) (2007) 6208–6218, doi: 10.1016/J.ACTAMAT.2007.07.029.
[78] V.B. Ozdol, C. Gammer, X.G. Jin, P. Ercius, C. Ophus, J. Ciston, A.M. Minor, Strain mapping at nanometer resolution using advanced nano-beam electron diffraction, Appl. Phys. Lett. 106 (25) (2015) 253107, doi: 10.1063/1.4922994.
[79] J. Wang, L. Ge, Z. Li, L. Li, Q. Guo, J. Li, Facile size-controlled synthesis of well-dispersed spherical amorphous alumina nanoparticles via homogeneous precipitation, Ceram. Int. 42 (7) (2016) 8545–8551, doi: 10.1016/j.ceramint.2016.02.081.
[80] A. Khalajhedayati, T.J. Rupert, Disruption of thermally-Stable nanoscale grain structures by strain localization, Sci. Rep. 5 (1) (2015) 10663, doi: 10.1038/srep10663.
[81] C. Schuh, T. Nieh, A survey of instrumented indentation studies on metallic glasses, J. Mater. Res. 19 (1) (2004) 46–57, doi: 10.1557/jmr.2004.19.1.46.
[82] R. Vaidyanathan, M. Dao, G. Ravichandran, S. Suresh, Study of mechanical deformation in bulk metallic glass through instrumented indentation, Acta Mater. 49 (18) (2001) 3781–3789, doi: 10.1016/S1359-6454(01)00263-4.
[83] R. Conner, R. Dandliker, W. Johnson, Mechanical properties of tungsten and steel fiber reinforced Zr41.25Ti13.75Cu12.5Ni10Be22.5 metallic glass matrix composites, Acta Mater. 46 (17) (1998) 6089–6102, doi: 10.1016/S1359-6454(98)00275-4.
[84] J.E. Carsley, W.W. Milligan, S.A. Hackney, E.C. Aifantis, Glasslike behavior in a nanostructured Fe/Cu alloy, Metall. Mater. Trans. A 26 (9) (1995) 2479–2481, doi: 10.1007/BF02671262.
[85] J.R. Trelewicz, C.A. Schuh, The Hall-Petch breakdown at high strain rates: optimizing nanocrystalline grain size for impact applications, Appl. Phys. Lett. 93 (17) (2008) 171916, doi: 10.1063/1.3000655.
[86] Y. Tong, T. Iwashita, W. Dmowski, H. Bei, Y. Yokoyama, T. Egami, Structural rejuvenation in bulk metallic glasses, Acta Mater. 86 (2015) 240–246, doi: 10.1016/J.ACTAMAT.2014.12.020.
[87] F. Meng, K. Tsuchiya, S. Seiichiro, Y. Yokoyama, Reversible transition of deformation mode by structural rejuvenation and relaxation in bulk metallic glass, Appl. Phys. Lett. 101 (12) (2012) 121914, doi: 10.1063/1.4753998.
[88] S.V. Ketov, Y.H. Sun, S. Nachum, Z. Lu, A. Checchi, A.R. Beraldin, H.Y. Bai, W.H. Wang, D.V. Louzguine-Luzgin, M.A. Carpenter, A.L. Greer, Rejuvenation of metallic glasses by non-affine thermal strain, Nature 524 (7564) (2015) 200–203, doi: 10.1038/nature14674.
[89] A.C. Lund, T.G. Nieh, C.A. Schuh, Tension/compression strength asymmetry in a simulated nanocrystalline metal, Phys. Rev. B 69 (1) (2004) 012101, doi: 10.1103/PhysRevB.69.012101.
[90] H. Van Swygenhoven, P. Derlet, A. Frøseth, Nucleation and propagation of dislocations in nanocrystalline fcc metals, Acta Mater. 54 (7) (2006) 1975–1983, doi: 10.1016/j.actamat.2005.12.026.
[91] N.Q. Vo, R.S. Averback, P. Bellon, S. Odunuga, A. Caro, Quantitative description of plastic deformation in nanocrystalline Cu: dislocation glide versus grain boundary sliding, Phys. Rev. B 77 (13) (2008) 134108, doi: 10.1103/PhysRevB.77.134108.
[92] G.J. Tucker, D.L. McDowell, Non-equilibrium grain boundary structure and inelastic deformation using atomistic simulations, Int. J. Plast. 27 (6) (2011) 841–857, doi: 10.1016/j.ijplas.2010.09.011.
[93] J. Lohmiller, R. Baumbusch, O. Kraft, P.A. Gruber, Differentiation of deformation modes in nanocrystalline pd films inferred from peak asymmetry evolution using insitu X-Ray diffraction, Phys. Rev. Lett. 110 (6) (2013) 066101, doi: 10.1103/PhysRevLett.110.066101.
[94] S.C. Pun, W. Wang, A. Khalajhedayati, J.D. Schuler, J.R. Trelewicz, T.J. Rupert, Nanocrystalline Al-Mg with extreme strength due to grain boundary doping, Mater. Sci. Eng.: A 696 (2017) 400–406, doi: 10.1016/J.MSEA.2017.04.095.
[95] R.J. Asaro, S. Suresh, Mechanistic models for the activation volume and rate sensitivity in metals with nanocrystalline grains and nano-scale twins, Acta Mater. 53 (12) (2005) 3369–3382, doi: 10.1016/J.ACTAMAT.2005.03.047.
[96] J. Lohmiller, M. Grewer, C. Braun, A. Kobler, C. Kübel, K. Schüler, V. Honkimäki, H. Hahn, O. Kraft, R. Birringer, P.A. Gruber, Untangling dislocation and grain boundary mediated plasticity in nanocrystalline nickel, Acta Mater. 65 (2014) 295–307, doi: 10.1016/j.actamat.2013.10.071.
[97] C.A. Bronkhorst, S.R. Kalidindi, L. Anand, Polycrystalline plasticity and the evolution of crystallographic texture in FCC metals, Philos. Trans. R. Soc. Lond. Ser. A: Phys. Eng. Sci. 341 (1662) (1992) 443–477, doi: 10.1098/rsta.1992.0111.
[98] J. Weissmüller, J. Ma.rkmann, Deforming nanocrystalline metals: new insights, new puzzles, Adv. Eng. Mater. 7 (4) (2005) 202–207, doi: 10.1002/adem.200400211.

[99] X. Zhou, N. Tamura, Z. Mi, J. Lei, J. Yan, L. Zhang, W. Deng, F. Ke, B. Yue, B. Chen, Reversal in the size dependence of grain rotation, Phys. Rev. Lett. 118 (9) (2017) 096101, doi: 10.1103/PhysRevLett.118.096101.
[100] B. Chen, K. Lutker, S.V. Raju, J. Yan, W. Kanitpanyacharoen, J. Lei, S. Yang, H.-R. Wenk, H.-k. Mao, Q. Williams, Texture of nanocrystalline nickel: probing the lower size limit of dislocation activity, Science 338 (6113) (2012) 1448–1451, doi: 10.1126/science.1228211.
[101] P.-L. Larsson, A. Giannakopoulos, E. SÖderlund, D. Rowcliffe, R. Vestergaard, Analysis of Berkovich indentation, Int. J. Solids Struct. 33 (2) (1996) 221–248, doi: 10.1016/0020-7683(95)00033-7.
[102] L. Min, C. Wei-min, L. Nai-gang, W. Ling-Dong, A numerical study of indentation using indenters of different geometry, J. Mater. Res. 19 (1) (2004) 73–78, doi: 10.1557/jmr.2004.19.1.73.
[103] M. Rittner, J. Weertman, J. Eastman, Structure-property correlations in nanocrystalline Al-Zr alloy composites, Acta Mater. 44 (4) (1996) 1271–1286, doi: 10.1016/1359-6454(95)00303-7.
[104] E.O. Hall, The deformation and ageing of mild steel: III discussion of results, Proc. Phys. Soc. Lond. Sect. B 64 (9) (1951) 747–753, doi: 10.1088/0370-1301/64/9/303.
[105] N.J. Petch, The cleavage strength of polycrystals, J. Iron Steel Inst. 173 (5) (1953) 25–28.
[106] J.W. Wyrzykowski, M.W. Grabski, The Hall-Petch relation in aluminium and its dependence on the grain boundary structure, Philos. Mag. A 53 (4) (1986) 505–520, doi: 10.1080/01418618608242849.
[107] D. Tabor, The Hardness of Metals, Clarendon Press, 2000.
[108] T. Uesugi, K. Higashi, First-principles studies on lattice constants and local lattice distortions in solid solution aluminum alloys, Comput. Mater. Sci 67 (2013) 1–10, doi: 10.1016/J.COMMATSCI.2012.08.037.
[109] G.-J.J. Gao, Y.-J. Wang, S. Ogata, Studying the elastic properties of nanocrystalline copper using a model of randomly packed uniform grains, Comput. Mater. Sci 79 (2013) 56–62, doi: 10.1016/J.COMMATSCI.2013.05.053.
[110] D. Feichtinger, P.M. Derlet, H. Van Swygenhoven, Atomistic simulations of spherical indentations in nanocrystalline gold, Phys. Rev. B 67 (2) (2003) 024113, doi: 10.1103/PhysRevB.67.024113.
[111] X. Chen, T. Richeton, C. Motz, S. Berbenni, Elastic fields due to dislocations in anisotropic bi- and tri-materials: applications to discrete dislocation pile-ups at grain boundaries, Int. J. Solids Struct. 164 (2019) 141–156, doi: 10.1016/j.ijsolstr.2019.01.020.
[112] ASM International. Handbook Committee. (2005). *ASM Handbook* (Vol. 2B). ASM International.
[113] W. Voigt, Ueber die Beziehung zwischen den beiden elasticitätsconstanten isotroper körper, Ann. Phys. 274 (12) (1889) 573–587, doi: 10.1002/andp.18892741206.
[114] J. Luo, A. Flewitt, S. Spearing, N. Fleck, W. Milne, Young's modulus of electroplated Ni thin film for MEMS applications, Mater. Lett. 58 (17–18) (2004) 2306–2309, doi: 10.1016/J.MATLET.2004.02.044.
[115] M. Öveçoğlu, M. Doerner, W. Nix, Elastic interactions of screw dislocations in thin films on substrates, Acta Metall. 35 (12) (1987) 2947–2957, doi: 10.1016/0001-6160(87)90294-X.